Mathematical Biosciences and Engineering

https://www.aimspress.com/journal/mbe

MBE, 23(5): 1203–1250
DOI: 10.3934/mbe.2026044
Received: 24 January 2026
Revised: 13 March 2026
Accepted: 20 March 2026
Published: 31 March 2026

Research article

Global well-posedness and pattern formation in a predator–prey reaction–diffusion system with prey-taxis

Mohamed Hafdane, Nossaiba Baba*and Saida Khiyar

Analysis, Modeling and Simulation Laboratory, Hassan II University, Morocco

* **Correspondence:** Email: noussaibababa1@gmail.com.

Abstract: This paper investigates a spatiotemporal predator–prey model that incorporates the Allee effect, the fear effect, prey-taxis, and harvesting within a Beddington–DeAngelis functional framework. The model captures the combined influence of biological interactions, behavioral responses, and harvesting activities on population dynamics in a spatially heterogeneous environment. The global existence, positivity, and boundedness of classical solutions are first established under appropriate parameter conditions. The existence and local stability of homogeneous steady states are then analyzed, and the conditions for diffusion-driven instability are derived to characterize the onset of spatial patterns. Using weakly nonlinear analysis, amplitude equations are developed to describe the modulation of spatial modes near the bifurcation threshold. Numerical investigations are conducted to complement the theoretical analysis: bifurcation diagrams are employed to examine the effects of biological parameters such as the Allee threshold (β), fear intensity (γ), and conversion efficiency (ε), while spatiotemporal simulations are performed to visualize different scenarios and demonstrate the impact of prey-taxis on pattern formation and population organization.

Keywords: predator-prey model; spatiotemporal dynamics; prey-taxis; turing instability; amplitude equation; pattern formation

---

1. Introduction

The study of population dynamics remains a cornerstone of biomathematics, offering critical insights into ecosystem functioning, species coexistence, and the formulation of ecological theory [1]. Over the decades, researchers have devoted significant effort to understanding how populations interact, respond to environmental changes, and evolve. Building on the pioneering predator–prey models introduced by Lotka and Volterra [2, 3], this area of research has expanded to encompass a wide range of theoretical extensions and practical applications, from conservation strategies to resource management.

Among all ecological systems, marine species represent some of the most sensitive organisms to environmental and anthropogenic perturbations. Due to their exposure to stressors such as chemical toxicity, overfishing, and climate variability, marine populations are particularly vulnerable to fluctuations in environmental quality and resource availability. Furthermore, these species are influenced by complex biological and behavioral mechanisms, including the Allee effect, fear effect, prey-taxis, and interspecific competition, which can substantially alter predator–prey dynamics and ecosystem stability.

To study how populations respond under both typical and unusual ecological conditions, researchers employ systems of differential equations that incorporate temporal and spatial dynamics. Mathematical modeling thus provides a rigorous and versatile framework for exploring the mechanisms governing population interactions. Over time, several biological processes have been incorporated into these models to better reflect the complexity of real-world ecosystems.

A key element in predator–prey theory is the predator's functional response, which defines how the predation rate varies with prey abundance and environmental context. This relationship is fundamental for understanding system stability, bifurcations, and the conditions enabling long-term coexistence of interacting species. Among the various forms proposed, the Beddington–DeAngelis functional response [4] has gained particular importance as it accounts for mutual interference among predators and the saturation effects at high prey density, providing a more realistic description of predation processes in natural environments. This formulation bridges the gap between the classical Holling type-II response and more complex behavioral interactions observed in marine ecosystems, where predator competition and prey refuge behaviors significantly influence energy transfer and population balance.

Beyond direct consumption, indirect ecological effects play a pivotal role in shaping species dynamics. The fear effect [5–7], for example, describes how prey modify their behavior in the presence of predators, allocating more time to vigilance or seeking refuge instead of feeding. Such behavioral shifts can lead to physiological stress, reduced energy intake, and lower reproductive success—sometimes producing a greater demographic impact than direct predation itself. The inclusion of fear mechanisms in predator–prey models has been shown to stabilize population oscillations and reveal complex nonlinear dynamics that better reflect observed ecological patterns.

Another key mechanism is prey-taxis, which describes the directed movement of predators toward regions of high prey density. This spatial process introduces heterogeneity in species distributions and can generate complex aggregation patterns or stabilize fluctuations depending on the intensity of taxis and diffusion rates [8–10]. Early contributions by Kareiva and Odell [11] laid the groundwork for modeling predator aggregation behavior, explaining how area-restricted search strategies lead to nonuniform spatial distributions consistent with empirical observations.

The integration of such behavioral and spatial mechanisms has inspired numerous theoretical advances. Recent studies [12–15] have explored the combined effects of diffusion, taxis, and predation intensity, revealing how these factors interact to produce or suppress spatiotemporal patterns. Reaction–diffusion models have proven particularly powerful for studying these processes, as they incorporate both random dispersal and directed movement, capturing the emergence of structures such as stripes, spots, and wave-like formations [16] and [17]. These complex spatial dynamics, first described in activator–inhibitor systems [18], have since been applied to ecological systems to explain pattern formation and self-organization in nature.

Finally, anthropogenic factors such as environmental toxicity and harvesting exert additional pressures on marine ecosystems. Toxic pollutants can increase mortality or reduce reproductive capacity in both prey and predators [19, 20], while intensive fishing disrupts trophic balance and may destabilize entire food webs [21, 22]. Understanding the interplay between these natural and human-induced processes is therefore crucial for predicting ecological resilience and guiding sustainable management strategies.

Reaction–diffusion mechanisms similar to those observed in ecological systems have also been explored in distributed electronic systems. For example, Arena et al. [23] demonstrated that two-layer cellular neural networks (CNNs) exhibit self-organization and pattern formation akin to activator–inhibitor dynamics. These studies highlight the broad applicability of diffusion-driven processes and suggest potential interdisciplinary insights, where theoretical frameworks developed in ecology can inform the design and analysis of electronic and computational systems.

Motivated by these findings, the present work investigates a model that describes a two-species system in which prey and predator dynamics are jointly influenced by ecological regulation, behavioral responses, spatial movement, toxicity, and harvesting pressures. Prey growth is modulated by an Allee effect, reflecting reproductive difficulties at low densities, and a fear effect, which reduces reproductive success in the presence of predators. Predator dynamics are governed by the Beddington–DeAngelis functional response, incorporating saturation and interference effects. Spatial heterogeneity is modeled through both diffusion and prey-taxis, where predators actively move toward prey concentrations. Additional mortality due to toxicity and harvesting represents environmental and anthropogenic stressors affecting both species. Our model is novel in simultaneously combining the Allee effect, fear effect, and prey-taxis within a Beddington–DeAngelis framework, which has not been previously explored in marine predator–prey systems. This synthesis reveals new dynamical regimes, including Turing-driven spatial heterogeneity, mixed stripe–spot patterns, and localized spot aggregates. It also clarifies how demographic thresholds (Allee effect) and behavioral modulation (fear, prey-taxis) interact to influence pattern formation, oscillations, and extinction risk, providing ecological insights beyond classical diffusion-driven models.

The subsequent sections of this paper are organized as follows. Section 2 presents the formulation and description of the proposed model. Section 3 establishes the global existence and boundedness of the solutions. Section 4 examines the homogeneous steady states. Section 5 analyzes the amplitude equations of the reaction–diffusion system near the onset of a Turing bifurcation. Section 6 presents numerical simulations illustrating the analytical results, and Section 7 concludes with a general discussion of the ecological implications.

2. Model description

We consider a spatiotemporal predator–prey system describing the interaction between a prey population $N(x,t)$ and a predator population $P(x,t)$ in a spatially heterogeneous marine environment. The model incorporates key ecological mechanisms, including density-dependent growth with Allee and fear effects, predator–prey interactions governed by a Beddington–DeAngelis functional response, toxicity-induced mortality, and harvesting pressure, in order to investigate the resulting spatiotemporal dynamics.

The prey population follows a growth law that combines the Allee effect and the fear effect. The Allee effect, expressed by the function $\frac{\alpha N}{\beta+N}$, captures the reproductive difficulties experienced by prey populations when their density is low, due to limited cooperation or mate availability. Here, α represents the maximum per capita reproductive rate, and β denotes the Allee threshold below which population growth becomes inefficient. The fear effect, modeled by the scaling factor $\frac{1}{1+\gamma P}$, reflects the behavioral changes of prey caused by the perceived risk of predation. The parameter γ quantifies the strength of this fear-induced response. When predators are abundant, prey spend more time hiding or avoiding risky areas, which reduces feeding and reproductive activity. As a result, the prey growth term is expressed as $N\left(\frac{\alpha N}{(\beta+N)(1+\gamma P)} - m_1 - \delta N\right)$, where m_1 denotes the natural mortality rate and δ represents the intraspecific competition rate among prey individuals [24].

Predator–prey interactions are governed by a Beddington–DeAngelis functional response, $\frac{aNP}{1+bN+cP}$, which accounts for both prey saturation at high densities and predator interference when predators become crowded. The parameter a measures the predation rate, b represents the prey saturation coefficient, and c denotes the predator interference coefficient. This formulation generalizes the classical Holling type II response by incorporating mutual interference among predators, which leads to a decrease in the per capita predation rate when predator density increases. The prey biomass decreases by $-\frac{aNP}{1+bN+cP}$, while predator biomass increases by $\varepsilon\frac{aNP}{1+bN+cP}$, where ε is the conversion efficiency of consumed prey into predator growth. The Beddington–DeAngelis functional response realistically represents marine predator-prey interactions:

- *Prey saturation (b):* captures the limited handling capacity of predators at high prey densities, preventing unrealistically high consumption rates.
- *Predator interference (c):* reflects competition among predators, where higher predator density reduces the per capita predation rate.

Together, these parameters allow the model to capture nonlinear feeding interactions and more realistic spatial and demographic effects observed in marine ecosystems.

Beyond classical biological interactions, exposure to environmental contaminants is a frequently observed factor in marine ecosystems. Prey species, which feed directly on environmental resources such as phytoplankton or suspended organic matter, are therefore directly exposed to toxic substances present in water or sediments. As prey density increases, spatial aggregation may enhance collective exposure and promote the local accumulation of pollutants. To capture this intensification associated with population concentration, toxicity-induced mortality of prey is modeled by the quadratic term $\mu_1 N^2$, representing a nonlinear density-dependent effect. Although both $-\delta N^2$ and $-\mu_1 N^2$ are quadratic in N, they describe biologically distinct mechanisms. The term $-\delta N^2$ represents classical intraspecific competition arising from limited resources and crowding effects, whereas $-\mu_1 N^2$ accounts for additional mortality caused by environmental toxicity, independent of direct competitive interactions. From a modeling perspective, these parameters can, in principle, be identified separately provided that toxicity-related effects are measurable experimentally or inferred from ecological observations, allowing one to distinguish between competition-driven and contamination-driven mortality processes.

Predators, in contrast, are primarily affected through the consumption of contaminated prey, leading to the transmission of toxins along the trophic chain. This bioaccumulation process acts proportionally to predator biomass and justifies the introduction of the linear term $\mu_2 P$. This formulation reflects mortality driven by indirect exposure to contaminants rather than by local aggregation effects.

Finally, human exploitation represents an additional pressure commonly present in marine ecosystems. It is incorporated into the model through the harvesting terms $E_1 N$ and $E_2 P$, which describe mortality proportional to the capture effort exerted on prey and predator populations.

Spatial heterogeneity is introduced through diffusion and cross-diffusion processes. The terms $d_1 \Delta N$ and $d_2 \Delta P$ represent random movement (diffusion) of prey and predators, respectively, where Δ is the Laplacian operator and d_1, d_2 are diffusion coefficients. Additionally, predators exhibit directed movement toward prey-rich regions, modeled by the prey-taxis term $-\eta\nabla \cdot (P\nabla N)$, where η is the prey-taxis sensitivity coefficient. A positive η implies that predators are attracted to regions with higher prey density, potentially leading to spatial aggregation and complex pattern formation. Combining these mechanisms, the spatiotemporal dynamics of prey and predator populations are governed by the following reaction–diffusion system:

$$\begin{cases} \dfrac{\partial N}{\partial t} = d_1 \Delta N + N\left(\frac{\alpha N}{(\beta+N)(1+\gamma P)} - m_1 - \delta N\right) - \frac{aNP}{1+bN+cP} - \mu_1 N^2 - E_1 N, & x \in \Omega,\ t > 0, \\ \dfrac{\partial P}{\partial t} = d_2 \Delta P - \eta\nabla \cdot (P\nabla N) - m_2 P + \frac{\varepsilon a NP}{1+bN+cP} - \mu_2 P - E_2 P, & x \in \Omega,\ t > 0, \\ \dfrac{\partial N(x,t)}{\partial \nu} = 0, \quad \dfrac{\partial P(x,t)}{\partial \nu} = 0, & x \in \partial\Omega,\ t > 0, \\ N(x,0) = N_0(x) \geq 0, \quad P(x,0) = P_0(x) \geq 0, & x \in \Omega. \end{cases} \tag{2.1}$$

Here, $\Omega \subset \mathbb{R}^n$ ($n \geq 1$) denotes a smooth bounded domain with smooth boundary $\partial\Omega$. The operator Δ represents the Laplacian in $\mathbb{R}^n$, and ν denotes the unit outward normal vector on $\partial\Omega$. The homogeneous Neumann boundary conditions $\frac{\partial N}{\partial \nu} = \frac{\partial P}{\partial \nu} = 0$ on $\partial\Omega$ express the absence of population flux across the boundary. The initial data $N_0(x)$, $P_0(x)$ are smooth nonnegative functions that are not identically zero. The model parameters are summarized in Table 1.

Table 1. Description and units of model parameters.

Parameter	Description	Units
d_1	Diffusion coefficient of prey	km^2/day
d_2	Diffusion coefficient of predator	km^2/day
η	Prey-taxis sensitivity coefficient	$\text{km}^4/$ (individual·day)
α	Maximum per capita reproductive rate of prey	day^{-1}
β	Allee threshold (prey density)	individuals/km^2
γ	Fear intensity parameter	$\text{km}^2/\text{individual}$
m_1	Natural mortality rate of prey	day^{-1}
m_2	Natural mortality rate of predator	day^{-1}
δ	Intraspecific competition coefficient (prey)	$\text{km}^2/$ (individual·day)
μ_1	Toxicity-induced mortality for prey	$\text{km}^2/$ (individual·day)
μ_2	Toxicity-induced mortality for predator	day^{-1}
a	Predation rate coefficient	$\text{km}^2/$ (individual·day)
b	Prey saturation coefficient	$\text{km}^2/\text{individual}$
c	Predator interference coefficient	$\text{km}^2/\text{individual}$
ε	Conversion efficiency	dimensionless
E_1	Harvesting effort on prey	day^{-1}
E_2	Harvesting effort on predator	day^{-1}

3. Global existence and boundedness of solution

This section aims to establish the local and global existence of solutions for system (2.1). For this purpose, the model is rewritten as follows:

$$\begin{cases} N_t = d_1\Delta N + h_1(N,P), \\ P_t = d_2\Delta P - \eta\nabla\cdot(P\nabla N) + h_2(N,P), \end{cases}$$

where

$$\begin{cases} h_1(N,P) = N\Big(\frac{\alpha N}{(\beta+N)(1+\gamma P)} - m_1 - \delta N\Big) - \frac{aNP}{1+bN+cP} - \mu_1 N^2 - E_1 N, \\ h_2(N,P) = -m_2 P + \frac{\varepsilon aNP}{1+bN+cP} - \mu_2 P - E_2 P. \end{cases}$$

In the rest of this paper, we shall work with this form of the system.

3.1. Local existence

Theorem 1. *Let $(N_0(x), P_0(x))$ be regular, nonnegative, and nontrivial initial data. Then, system (2.1) admits a classical solution $(N(x,t), P(x,t))$ satisfying the following properties:*

*(1) **(Local existence and strict positivity.)** There exists a maximal time $T_{\max} > 0$ and a unique solution*

$$(N,P) \in \left[C([0,T_{\max}); W^{1,p}(\Omega)) \cap C^{2,1}(\Omega\times(0,T_{\max}))\right]^2,$$

such that

$$N(x,t) > 0, \quad P(x,t) > 0, \quad \forall (x,t) \in \Omega\times(0,T_{\max}),\ t > 0.$$

*(2) (L^∞ **bound for** N.) There exists a constant $C_1 > 0$ such that*

$$0 < N(x,t) \le C_1, \quad \forall (x,t) \in \Omega\times(0,T_{\max}).$$

*(3) (L^1 **bound for** P.) There exists a constant $C_2 > 0$, independent of time, such that*

$$0 < \|P(\cdot,t)\|_{L^1(\Omega)} \le C_2, \quad \forall t \in (0,T_{\max}).$$

Proof. **1). Local existence and strict positivity.**

Let $U = (N,P)$. The system can be rewritten in the compact form

$$U_t = \nabla\cdot(D(U)\nabla U) + \mathcal{H}(U),$$

where

$$D(U) = \begin{pmatrix} d_1 & 0 \\ -\eta P & d_2 \end{pmatrix}, \qquad \mathcal{H}(U) = \begin{pmatrix} h_1(N,P) \\ h_2(N,P) \end{pmatrix}.$$

According to the theorem of Amann [25], there exists a local classical solution.
For the second equation of P, we have

$$\partial_t P - d_2\Delta P + \eta\nabla\cdot(P\nabla N) = h_2(N,P), \quad x\in\Omega,\ t>0,$$

with the initial condition $P(x, 0) = P_0(x) \geq 0$. Since 0 is a subsolution, the maximum principle implies $P(x, t) \geq 0$. If $P_0 \not\equiv 0$, the strong maximum principle ensures that $P(x, t) > 0$ for all $t > 0$.
Similarly, for the first equation of N,

$$\partial_t N - d_1 \Delta N = h_1(N, P),$$

we obtain $N(x, t) \geq 0$, and if $N_0 \not\equiv 0$, then $N(x, t) > 0$ for all $t > 0$.

2). L^∞ bound for N.

The prey equation can be written as

$$\partial_t N = d_1 \Delta N + h_1(N, P).$$

By ignoring the unfavorable terms, we obtain

$$\partial_t N \leq d_1 \Delta N + N(\alpha - m_1 - \delta N).$$

By comparison with the corresponding logistic equation, it follows that

$$0 < N(x, t) \leq \max\left\{ \|N_0\|_{L^\infty(\Omega)}, \ \frac{\alpha - m_1}{\delta} \right\} =: C_1.$$

3). L^1 bound for P

Define

$$n(t) = \int_\Omega N(x, t)\, dx, \qquad p(t) = \int_\Omega P(x, t)\, dx.$$

Integrating the system equations over Ω and using the homogeneous Neumann boundary conditions, we obtain

$$\frac{d}{dt}(\varepsilon n(t) + p(t)) \leq -m_2(\varepsilon n(t) + p(t)) + \varepsilon(\alpha + m_2) C_1 |\Omega|.$$

Set $y(t) = \varepsilon n(t) + p(t)$, then the inequality can be written as $y'(t) \leq -m_2 y(t) + C$. Applying Gronwall's lemma yields

$$y(t) \leq y(0) e^{-m_2 t} + \frac{C}{m_2}(1 - e^{-m_2 t}).$$

Hence,

$$p(t) \leq \varepsilon \|N_0\|_{L^1(\Omega)} + \|P_0\|_{L^1(\Omega)} + \frac{\varepsilon(\alpha + m_2) C_1 |\Omega|}{m_2} =: C_2.$$

□

3.2. Global existence

Theorem 2. *[Global existence of the classical solution] Let $\Omega \subset \mathbb{R}^n$ be a bounded domain with smooth boundary $\partial\Omega$. Assume that the initial data $(N_0(x), P_0(x)) \in [W^{1,p}(\Omega)]^2$ for some $p > n$, and that $N_0(x) \geq 0$, $P_0(x) \geq 0$ for all $x \in \overline{\Omega}$. If*

$$0 < \eta \leq \frac{d_1 d_2}{3(n + 2)(d_1 + d_2) C_1},$$

then system (2.1) admits a unique global classical solution $(N(x,t), P(x,t)) \in \left[C([0,\infty); W^{1,p}(\Omega)) \cap C^{2,1}(\overline{\Omega} \times (0,\infty))\right]^2$*, and there exists a positive constant M, depending only on the initial data* $N_0(x)$ *and* $P_0(x)$*, such that*

$$\|N(\cdot,t)\|_{L^\infty(\Omega)} + \|P(\cdot,t)\|_{L^\infty(\Omega)} \leq M, \qquad \forall t \geq 0.$$

The upper bound on the prey-taxis coefficient η in Theorem 2 has a clear biological meaning. Excessively strong predator attraction to prey can lead to very high local prey densities, potentially causing unrealistic aggregation or blow-up in the model. Ecologically, moderate prey-taxis promotes spatial pattern formation, while overly strong prey-taxis may destabilize the system. Hence, the bound on η ensures both global existence of solutions and ecological realism.

When the prey-taxis coefficient η is low, predators have limited ability to detect and follow prey density gradients. This weak sensitivity prevents effective spatial regulation of local prey accumulations, allowing small initial heterogeneities to gradually amplify and form persistent spatial structures. Biologically, this corresponds to a system where predator adaptive behavior is insufficient to stabilize population distributions.

At intermediate values of η, predator movement becomes sufficiently efficient to compensate for local imbalances. High-density prey patches are exploited more rapidly, suppressing the amplification of spatial fluctuations. The system then maintains a more homogeneous distribution, promoting stable coexistence of both species. In this regime, predator search behavior plays a regulatory role that supports long-term population persistence.

Conversely, when η becomes too high, predator sensitivity to prey gradients is excessive. Such hypersensitivity leads to rapid and massive aggregations, which can cause repeated local overexploitation and significant spatial imbalances. Biologically, this behavior represents unrealistic dynamics, inconsistent with stability observed in natural marine ecosystems. Therefore, the upper bound imposed on η in Theorem 2 can be interpreted as an ecological constraint necessary to prevent overreactive predator behavior that would threaten system viability.

Next, we recall several preliminary results that will be useful in the subsequent analysis. In particular, we summarize some classical estimates concerning the diffusion semigroup associated with homogeneous Neumann boundary conditions (see [26]). Let $p \in (1,\infty)$ and define the operator $A := -\Delta$ by

$$D(A) := \left\{ \omega \in W^{2,p}(\Omega) \ : \ \frac{\partial \omega}{\partial n} = 0 \text{ on } \partial\Omega \right\}.$$

It is well known that A is a sectorial operator in $L^p(\Omega)$, and that $-A$ generates an analytic semigroup $\{e^{-tA}\}_{t\geq 0}$ on $L^p(\Omega)$. Similarly, for each $d_i > 0$ $(i = 1, 2)$, we define $A_{d_i} := -d_i\Delta$, which enjoy the same properties. These operators will serve as the main tools for deriving the regularity estimates required in the forthcoming analysis of the system.

Lemma 1. *Assume that* $r \in [0,1)$, $p \in [1,\infty]$*, and* $q \in (1,\infty)$*. Then, there exists some positive constant* C_3 *such that*

$$\|P\|_{r,p} \leq C_3 \|(A+1)^\theta P\|_{L^q}, \tag{3.1}$$

for any $P \in D((A+1)^\theta)$ *where* $\theta \in (0,1)$ *satisfies*

$$r - \frac{n}{p} < 2\theta - \frac{n}{q}.$$

If in addition $q \geq p$, *then there exist* $C_4 > 0$ *and* $\gamma > 0$ *such that for any* $P \in L^p(\Omega)$,

$$\|(A+1)^{\theta} e^{-t(A+1)} P\|_{L^q} \leq C_4 \, t^{-\theta-\frac{n}{2}\left(\frac{1}{p}-\frac{1}{q}\right)} e^{-\gamma t} \|P\|_{L^p}, \tag{3.2}$$

where the associated diffusion semigroup $\{e^{-t(A+1)}\}_{t\geq 0}$ *maps* $L^p(\Omega)$ *into* $D((A+1)^{\theta})$. *Moreover, for any* $p \in (1,\infty)$ *and* $\varepsilon > 0$, *there exist* $C_5 > 0$ *and* $\mu > 0$ *such that*

$$\|(A+1)^{\theta} e^{-tA} \nabla \cdot P\|_{L^p} \leq C_5 \, t^{-\theta-\frac{1}{2}} e^{-\mu t} \|P\|_{L^p}, \tag{3.3}$$

which is valid for all $\mathbb{R}^n$*-valued* $P \in L^p(\Omega)$.

Lemma 2. *There exists a constant* $C_6 > 0$ *such that for all* $P \in W^{1,q}(\Omega)$,

$$\|P\|_{L^p} \leq C_6 \|P\|_{L^q}^{\kappa} \|P\|_{L^r}^{1-\kappa}, \tag{3.4}$$

where $p, q \geq 1$ *satisfy* $p(n-q) < nq$, $r \in (0,p)$, *with*

$$\kappa = \frac{\frac{n}{r} - \frac{n}{p}}{\frac{n}{r} + 1 - \frac{n}{q}} \in (0,1).$$

Lemma 3. *There exists a constant* $C_7 > 0$ *such that for all* $P \in W^{1,q}(\Omega)$,

$$\|P\|_{1,p} \leq C_7 (\|\nabla P\|_{L^p} + \|P\|_{L^q}), \tag{3.5}$$

where $p > 1$ *and* $q > 0$.

Finally, we recall the following elementary inequality.

Lemma 4. *Assume that* $x(t) \geq 0$ *satisfies*

$$\begin{cases} x'(t) \leq -c_1 x^r(t) + c_2 x(t) + c_3, \quad t > 0, \\ x(0) = x_0, \end{cases} \tag{3.6}$$

where $a_1, c_2, c_3 > 0$ *and* $r > 1$. *Then, there exist constants* $a_1(x_0)$ *and* $a_2(c_1, c_2, c_3, r)$ *such that*

$$x(t) \leq \max\{a_1(x_0),\ a_2(c_1, c_2, c_3, r)\}. \tag{3.7}$$

Lemma 5. *Let* $\Omega \subset \mathbb{R}^n$ *be a bounded domain with smooth boundary* $\partial\Omega$. *Assume that the initial data* $(N_0(x), P_0(x)) \in [W^{1,p}(\Omega)]^2$ *for some* $p > n$, *and that* $N_0(x) \geq 0$, $P_0(x) \geq 0$ *for all* $x \in \overline{\Omega}$. *If*

$$0 \leq \eta \leq \frac{d_1 d_2}{3(n+2)(d_1+d_2)C_1},$$

then there exists a positive constant C_{10} *such that*

$$\|P(\cdot,t)\|_{L^{n+2}(\Omega)} \leq C_{10}, \qquad \forall t \in (0, T_{\max}).$$

Proof. Let $\Omega \subset \mathbb{R}^n$ and set $m = n + 2$. Let $\rho > 0$ be a constant defined by

$$\rho = \frac{1}{C_1\,(d_1 + d_2)}\sqrt{\frac{d_1 d_2 (m-1)}{6m}}.$$

Define the auxiliary function $\Psi(N) = e^{(\rho N)^2}$. Then, we have

$$\begin{cases} \Psi'(N) = 2\rho^2 N \Psi(N), \\ \Psi''(N) = 2\rho^2(1 + 2\rho^2 N^2)\Psi(N), \\ 1 \le e^{(\rho N)^2} \le e^{(\rho C_1)^2}, \quad \forall (x,t) \in \Omega \times (0, T_{\max}). \end{cases} \tag{3.8}$$

To derive the L^m-estimate for P, we start by differentiating $\int_\Omega P^m \Psi(N)\,dx$ with respect to time:

$$\begin{aligned} \frac{1}{m}\frac{d}{dt}\int_\Omega P^m\Psi(N)\,dx &= \int_\Omega P^{m-1}\Psi(N)\,P_t\,dx + \int_\Omega P^m\Psi'(N)\,N_t\,dx \\ &= d_2\int_\Omega P^{m-1}\Psi(N)\Delta P\,dx - \eta\int_\Omega P^{m-1}\Psi(N)\,\nabla\cdot(P\nabla N)\,dx \\ &\quad + \int_\Omega P^{m-1}\Psi(N)\,h_2(N,P)\,dx + \frac{d_1}{m}\int_\Omega P^m\Psi'(N)\Delta N\,dx \\ &\quad + \frac{1}{m}\int_\Omega P^m\Psi'(N)h_1(N,P)\,dx \\ &= -d_2(m-1)\int_\Omega P^{m-2}\Psi(N)\,|\nabla P|^2\,dx - d_2\int_\Omega P^{m-1}\Psi'(N)\,\nabla N\cdot\nabla P\,dx \\ &\quad + \eta(m-1)\int_\Omega P^{m-1}\Psi(N)\,\nabla N\cdot\nabla P\,dx + \eta\int_\Omega P^m\Psi'(N)|\nabla N|^2\,dx \\ &\quad - d_1\int_\Omega P^{m-1}\Psi'(N)\,\nabla N\cdot\nabla P\,dx - \frac{d_1}{m}\int_\Omega P^m\Psi''(N)|\nabla N|^2\,dx \\ &\quad + \int_\Omega P^{m-1}\Psi(N)h_2(N,P)\,dx + \frac{1}{m}\int_\Omega P^m\Psi'(N)h_1(N,P)\,dx. \end{aligned}$$

We have $h_1(N,P) \le \alpha N$ and $h_2(N,P) \le \dfrac{\varepsilon a}{b}P$. Hence,

$$\begin{aligned} \frac{1}{m}\frac{d}{dt}\int_\Omega P^m\Psi(N)\,dx \le &-d_2(m-1)\int_\Omega P^{m-2}\Psi(N)\,|\nabla P|^2\,dx \\ &- (d_1+d_2)\int_\Omega P^{m-1}\Psi'(N)\,\nabla N\cdot\nabla P\,dx \\ &+ \eta(m-1)\int_\Omega P^{m-1}\Psi(N)\,\nabla N\cdot\nabla P\,dx \\ &+ \eta\int_\Omega P^m\Psi'(N)\,|\nabla N|^2\,dx \\ &- \frac{d_1}{m}\int_\Omega P^m\Psi''(N)\,|\nabla N|^2\,dx \end{aligned}$$

$$+\left(\frac{\varepsilon a}{b}+\frac{2\rho^2\alpha C_1^2}{m}\right)\int_\Omega P^m\Psi(N)\,dx.$$

By moving all nonnegative terms to the left-hand side, we obtain

$$\begin{aligned}\frac{1}{m}\frac{d}{dt}\int_\Omega P^m\Psi(N)\,dx\ &+d_2(m-1)\int_\Omega P^{m-2}\Psi(N)\,|\nabla P|^2\,dx+\frac{d_1}{m}\int_\Omega P^m\Psi''(N)\,|\nabla N|^2\,dx\\ &\le -(d_1+d_2)\int_\Omega P^{m-1}\Psi'(N)\,\nabla N\cdot\nabla P\,dx\\ &\quad+\eta(m-1)\int_\Omega P^{m-1}\Psi(N)\,\nabla N\cdot\nabla P\,dx\\ &\quad+\eta\int_\Omega P^m\Psi'(N)\,|\nabla N|^2\,dx\\ &\quad+\left(\frac{\varepsilon a}{b}+\frac{2\rho^2\alpha C_1^2}{m}\right)\int_\Omega P^m\Psi(N)\,dx.\end{aligned}$$

The mixed gradient terms can be controlled using Young's inequality together with the specific choice of ρ and the smallness condition on η. The detailed calculations are given in Appendix A.1. Consequently, we obtain

$$\frac{1}{m}\frac{d}{dt}\int_\Omega P^m\Psi(N)\,dx+\frac{d_2(m-1)}{2}\int_\Omega P^{m-2}\Psi(N)\,|\nabla P|^2\,dx\le C_8\int_\Omega P^m\Psi(N)\,dx,\tag{3.9}$$

where $C_8=\frac{\varepsilon a}{b}+\frac{2\rho^2\alpha C_1^2}{m}$. By a Gagliardo–Nirenberg interpolation argument (see Appendix A.2), we obtain

$$\int_\Omega P^m\Psi(N)\le C(\|\nabla P^{m/2}\|_2^2+1)^\kappa\tag{3.10}$$

for some $\kappa\in(0,1)$. Consequently (see Appendix A.2),

$$\int_\Omega P^{m-2}\Psi(N)|\nabla P|^2\ge C\left(\int_\Omega P^m\Psi(N)\right)^{1/\kappa}-C.\tag{3.11}$$

Hence from (3.9) and (A.2), we obtain

$$\frac{1}{m}\frac{d}{dt}\int_\Omega P^m\Psi(N)\le-\frac{2(m-1)}{m^2C_9^{\frac{1}{\kappa}}}\left(\int_\Omega P^m\Psi(N)\right)^{\frac{1}{\kappa}}+C_8\int_\Omega P^m\Psi(N)+\frac{2(m-1)}{m^2}\tag{3.12}$$

for all $t\in(0,T_{\max})$, where $1/\kappa>1$. By using Lemma 4, we conclude that there exists a constant $C_{10}>0$ such that

$$\|P(\cdot,t)\|_m\le\left(\int_\Omega P^m\Psi(N)\right)^{\frac{1}{m}}\le C_{10},\quad \text{for all } t\in(0,T_{\max}),\tag{3.13}$$

which is the desired result. □

Lemma 6. *Let $\Omega\subset\mathbb{R}^n$ be a bounded domain with smooth boundary $\partial\Omega$. Assume that the initial data $(N_0(x),P_0(x))\in[W^{1,p}(\Omega)]^2$ for some $p>n$, and that $N_0(x)\ge0$ and $P_0(x)\ge0$ for all $x\in\overline{\Omega}$. If*

$$0<\eta\le\frac{d_1d_2}{3(n+2)(d_1+d_2)C_1},$$

then there exists a positive constant C_{19} *such that*

$$\|P(\cdot,t)\|_{L^\infty(\Omega)} \le C_{19}, \qquad \forall t \in (0, T_{\max}).$$

Proof. We use semigroup arguments (see, e.g., [26]) to derive the L^∞-bound of N. Specifically, we show that for any $\tau \in (0, T_{\max})$, there exists a constant $F(\tau) > 0$ such that $\|N(\cdot,t)\|_{W^{1,\infty}(\Omega)} \le F(\tau)$ for all $t \in (0,\tau)$. Let $q = n + 2$. From the first equation of system (2.1), we have

$$\frac{dN}{dt} = d_1 \Delta N - N + (h_1(N,P) + N).$$

Then, by the variation-of-constants formula, we obtain

$$N(\cdot,t) = e^{-t\,(A_{d_1}+1)}\, N_0 + \int_0^t e^{-(t-s)\,(A_{d_1}+1)} (h_1(N,P) + N)\, ds.$$

Therefore, according to Lemma 1, we obtain

$$\begin{aligned}\|N(\cdot,t)\|_{W^{1,\infty}(\Omega)} &\le C_3\, \|(A_{d_1}+1)^\theta N(\cdot,t)\|_{L^q(\Omega)} \\ &\le C_3 C_4\, t^{-\theta} e^{-\gamma t} \|N_0\|_{L^q(\Omega)} + C_3 C_4 \int_0^t (t-s)^{-\theta} e^{-\gamma(t-s)} \|h_1(N,P) + N\|_{L^q(\Omega)}\, ds.\end{aligned}$$

Moreover, we have

$$\|h_1(N,P) + N\|_{L^q(\Omega)} \le \left[\left(1 + \alpha + m_1 + \frac{a}{c} + E_1\right) C_1 + (\delta + \mu_1) C_1^2\right] |\Omega|^{\frac{1}{q}}.$$

Consequently, it follows that

$$\|N(\cdot,t)\|_{W^{1,\infty}(\Omega)} \le C_{11}\, t^{-\theta} + C_{12} \int_0^t (t-s)^{-\theta} e^{-\gamma(t-s)}\, ds.$$

Setting $\sigma = t - s$ gives

$$\begin{aligned}\|N(\cdot,t)\|_{W^{1,\infty}(\Omega)} &\le C_{11}\, \tau^{-\theta} + C_{12} \int_0^\infty \sigma^{-\theta} e^{-\gamma\sigma}\, d\sigma \\ &\le C_{11}\, \tau^{-\theta} + C_{12}\, \Gamma(1-\theta),\end{aligned} \tag{3.14}$$

where $\Gamma(\cdot)$ denotes the Gamma function. Next, applying the variation-of-constants formula, we obtain

$$\begin{aligned}P(\cdot,t) = e^{-t(A_{d_2}+1)} P_0 &+ \eta \int_0^t e^{-(t-s)(A_{d_2}+1)} \nabla\cdot(P\nabla N)\, ds \\ &+ \int_0^t e^{-(t-s)(A_{d_2}+1)} (h_2(N,P) + P)\, ds.\end{aligned}$$

For convenience, we decompose $P(\cdot,t)$ as follows:

$$P_1(\cdot,t) = e^{-t(A_{d_2}+1)} P_0,$$

$$P_2(\cdot,t) = \eta \int_0^t e^{-(t-s)(A_{d_2}+1)} \nabla\cdot(P\nabla N)\, ds,$$

$$P_3(\cdot,t) = \int_0^t e^{-(t-s)(A_{d_2}+1)} (h_2(N,P) + P)\, ds.$$

Thus, we can write

$$P(\cdot,t) = P_1(\cdot,t) + P_2(\cdot,t) + P_3(\cdot,t).$$

Hence, using the semigroup estimates for P_1, P_2, and P_3 (see Appendix B), we obtain

$$\|P(\cdot,t)\|_{L^\infty(\Omega)} \le C_{19} := C_{13}\tau^{-\xi}\|P_0\|_{L^\infty(\Omega)} + C_{16}\,\Gamma\Big(\tfrac{1}{2} - \varrho - \varepsilon\Big) + C_{18}\,\Gamma(1-\varsigma), \qquad \forall\, t \in (0, T_{\max}).$$

□

Proof of Theorem 2. From Theorem 1, we have $N(x,t) \le C_1$ for all $(x,t) \in \Omega \times (0, T_{\max})$. Moreover, Lemma 6 yields $\|P(\cdot,t)\|_{L^\infty(\Omega)} \le C_{19}$. Hence, there exists a constant $M > 0$ depending only on the initial data (N_0, P_0) such that

$$\|N(\cdot,t)\|_{L^\infty(\Omega)} + \|P(\cdot,t)\|_{L^\infty(\Omega)} \le M, \qquad N_0(x), P_0(x) \ge 0,\ N_0, P_0 \not\equiv 0.$$

This completes the proof of Theorem 2. □

4. Homogeneous steady states

In this section, we analyze the spatially homogeneous steady states and investigate their stability under the influence of the prey-taxis sensitivity coefficient η. The first step is to determine the coexistence equilibrium, which represents a positive steady state ensuring the simultaneous persistence of both species. Then, the local stability of this equilibrium will be examined to identify the effect of prey-taxis on the system dynamics.

4.1. Existence of homogeneous steady states

The homogeneous steady states correspond to constant equilibrium solutions of system (2.1), denoted by $E^*(N^*, P^*)$. These equilibria satisfy the following system:

$$\begin{cases} \left(\dfrac{\alpha N^*}{(\beta + N^*)(1+\gamma P^*)} - m_1 - \delta N^*\right) - \dfrac{a P^*}{1 + bN^* + cP^*} - \mu_1 N^* - E_1 = 0, \\ -m_2 + \dfrac{\varepsilon a N^*}{1 + bN^* + cP^*} - \mu_2 - E_2 = 0. \end{cases} \tag{4.1}$$

From the second equation of system (4.1), we obtain

$$P^* = \frac{1}{c}\left(\frac{\varepsilon a N^*}{K} - 1 - bN^*\right), \qquad K := m_2 + \mu_2 + E_2. \tag{4.2}$$

Substituting this expression into the first equation of (4.1) and performing some simplifications, we obtain a quartic polynomial equation:

$$A_4 N^{*4} + A_3 N^{*3} + A_2 N^{*2} + A_1 N^* + A_0 = 0,$$

where the positive roots correspond to biologically admissible equilibrium values N^*. The corresponding predator density P^* can then be determined from (4.2). The coefficients A_i are expressed as

$$\begin{aligned}
A_4 &= -\frac{c\varepsilon^2\gamma a(\delta+\mu_1)}{K} + c\varepsilon\gamma b(\delta+\mu_1),\\
A_3 &= -c^2\epsilon(\delta+\mu_1) + c\epsilon\gamma(\delta+\mu_1) - \frac{c\epsilon^2\beta\gamma a(\delta+\mu_1)}{K} + c\epsilon\beta\gamma b(\delta+\mu_1) - \frac{\gamma\epsilon^2 a^2}{K} + 2\gamma\epsilon ab\\
&\quad - \gamma b^2 K - \frac{c\epsilon^2\gamma a(m_1+E_1)}{K} + c\epsilon\gamma b(m_1+E_1),\\
A_2 &= \alpha c^2\varepsilon - c^2\varepsilon\beta(\delta+\mu_1) + c\varepsilon\gamma\beta(\delta+\mu_1) - c^2\varepsilon(m_1+E_1) + c\varepsilon\gamma(m_1+E_1) - ac\varepsilon + 2a\gamma\varepsilon\\
&\quad + bK(c-\gamma) - \frac{c\varepsilon^2\beta\gamma a(m_1+E_1)}{K} - \frac{\varepsilon^2\beta\gamma a^2}{K} + \beta\gamma bc\varepsilon(m_1+E_1) + \beta\gamma ba - \gamma bK,\\
A_1 &= -c^2\varepsilon\beta(m_1+E_1) + c\varepsilon\gamma\beta(m_1+E_1) - ac\varepsilon\beta + a\gamma\varepsilon\beta + (\beta b+1)K(c-\gamma) + \beta(\gamma\varepsilon a - \gamma bK),\\
A_0 &= \beta K(c-\gamma).
\end{aligned}$$

The nature of the roots of this quartic equation depends on the sign of its discriminant [27]. A sufficient condition ensuring the existence of at least one positive equilibrium N^* is given by

$$A_0 < 0 \quad \Longleftrightarrow \quad c < \gamma.$$

Therefore, system (2.1) admits at least one biologically feasible equilibrium whenever $c < \gamma$.

4.2. Stability of homogeneous steady states

We now analyze the local stability of the coexistence equilibrium $E^*(N^*, P^*)$ under the influence of the prey-taxis parameter η. Let small perturbations be introduced around the steady state as $N(x,t) = N^* + \tilde{N}(x,t)$ and $P(x,t) = P^* + \tilde{P}(x,t)$, where $(\tilde{N}, \tilde{P})$ denote infinitesimal deviations from equilibrium. By substituting these expressions into system (2.1) and retaining only the first-order terms, the linearized form of the system can be written as

$$\frac{\partial}{\partial t}\begin{pmatrix}\tilde{N}\\ \tilde{P}\end{pmatrix} = J\begin{pmatrix}\tilde{N}\\ \tilde{P}\end{pmatrix} + D\Delta\begin{pmatrix}\tilde{N}\\ \tilde{P}\end{pmatrix},$$

where

$$J = \begin{pmatrix} j_{11} & j_{12}\\ j_{21} & j_{22}\end{pmatrix}, \qquad D = \begin{pmatrix} d_1 & 0\\ -\eta P^* & d_2\end{pmatrix}.$$

The entries of the Jacobian matrix J, evaluated at the steady state $E^*(N^*, P^*)$, are given by

$$\begin{aligned}
j_{11} &= \frac{\alpha N^{*2} + 2\alpha\beta N^*}{(1+\gamma P^*)(N^*+\beta)^2} - \frac{aP^* + acP^{*2}}{(1+bN^*+cP^*)^2} - 2(\delta+\mu_1)N^* - m_1 - E_1,\\
j_{12} &= -\frac{\alpha\gamma N^{*2}}{(1+\gamma P^*)^2(N^*+\beta)} - \frac{aN^* + abN^{*2}}{(1+bN^*+cP^*)^2},
\end{aligned}$$

$$j_{21} = \frac{\varepsilon a P^* + \varepsilon a c P^{*2}}{(1 + bN^* + cP^*)^2},$$

$$j_{22} = -(m_2 + \mu_2 + E_2) + \frac{\varepsilon a N^* + \varepsilon a b N^{*2}}{(1 + bN^* + cP^*)^2}.$$

In this analysis, we consider a two-dimensional bounded spatial domain $\Omega = [0, L] \times [0, L] \subset \mathbb{R}^2$, which represents a typical ecological habitat. This choice is particularly relevant since two-dimensional domains are sufficient to capture the main spatial organizations observed in biological systems. The boundary of the domain is assumed to be impermeable for both species, that is, homogeneous Neumann boundary conditions are imposed: $\partial_\nu \tilde{N} = \partial_\nu \tilde{P} = 0$ on $\partial\Omega$, meaning that no flux of individuals crosses the boundary. We then look for normal mode perturbations of the form

$$\begin{pmatrix} \tilde{N}(x,t) \\ \tilde{P}(x,t) \end{pmatrix} = \mathbf{v}\, e^{\lambda t}\, \phi(x),$$

where $\mathbf{v} \in \mathbb{R}^2$ is an eigenvector and $\phi(x)$ is an eigenfunction of the Laplacian satisfying $\Delta\phi + k^2\phi = 0$ and $\partial_\nu \phi = 0$ on $\partial\Omega$. The corresponding eigenvalues are given by $k^2 = \frac{m^2\pi^2}{L^2} + \frac{n^2\pi^2}{L^2}$, with $m, n \in \mathbb{N}$. For each admissible spatial mode k, the linearized system reduces to

$$\frac{d\mathbf{v}}{dt} = (J - D_k)\mathbf{v}, \qquad D_k = -\,k^2 D,$$

leading to the spectral problem $\det(\lambda I - J - D_k) = 0$, i.e.,

$$\begin{vmatrix} \lambda - j_{11} + d_1 k^2 & -j_{12} \\ -\, j_{21} - \eta P^* k^2 & \lambda - j_{22} + d_2 k^2 \end{vmatrix} = 0.$$

Expanding the determinant gives a quadratic equation in λ:

$$\lambda^2 + A_k \lambda + B_k = 0, \tag{4.3}$$

with

$$A_k = (d_1 + d_2)k^2 - (j_{11} + j_{22}),$$

$$B_k = d_1 d_2 k^4 - (d_1 j_{22} + d_2 j_{11} + \eta P^* j_{12})k^2 + \det(J).$$

The following theorem provides the conditions under which the homogeneous equilibrium $E^*(N^*, P^*)$ is stable or unstable depending on the prey-taxis parameter η.

Theorem 3. *Let* (N^*, P^*) *be a positive homogeneous equilibrium of system* (2.1). *Assume that the following condition holds:* (H1) $j_{11} + j_{22} < 0$ *and* $\det(J) > 0$, *which ensures that the equilibrium is locally asymptotically stable in the absence of diffusion.*

(i) If $d_1 j_{22} + d_2 j_{11} < 2\sqrt{d_1 d_2 \det(J)}$, *then* (N^*, P^*) *remains locally asymptotically stable for all* $\eta \geq 0$, *and no Turing instability can arise.*

(ii) If $d_1 j_{22} + d_2 j_{11} > 2\sqrt{d_1 d_2 \det(J)}$, *then there exists a critical prey-taxis coefficient*

$$\eta_c^* = \frac{d_1 j_{22} + d_2 j_{11} - 2\sqrt{d_1 d_2 \det(J)}}{-P^* j_{12}},$$

such that

$$\begin{cases} 0 < \eta < \eta_c^* & \Rightarrow (N^*, P^*) \textit{ becomes unstable and a Turing bifurcation occurs}, \\ \eta = \eta_c^* & \Rightarrow \textit{a critical bifurcation arises for } k_c^2 = \frac{d_1 j_{22} + d_2 j_{11} + \eta_c^* P^* j_{12}}{2 d_1 d_2}, \\ \eta > \eta_c^* & \Rightarrow (N^*, P^*) \textit{ recovers its stability and spatial patterns disappear.} \end{cases}$$

Proof. For $k = 0$, the characteristic equation reduces to

$$\lambda^2 - (j_{11} + j_{22})\lambda + \det(J) = 0.$$

According to the Routh–Hurwitz criterion, all eigenvalues have negative real parts if and only if assumption (H1) holds. Therefore, in the absence of diffusion and prey-taxis effects ($k = 0$), the homogeneous equilibrium (N^*, P^*) is locally asymptotically stable.

For $k > 0$. From the characteristic equation (4.3), we note that since $d_1, d_2 > 0$, the leading coefficient of B_k is positive. Hence, B_k is a convex quadratic function of k^2, attaining its minimum at

$$k_c^2 = \frac{d_1 j_{22} + d_2 j_{11} + \eta P^* j_{12}}{2 d_1 d_2},$$

with the minimum value

$$B_{k_c} = \det(J) - \frac{(d_1 j_{22} + d_2 j_{11} + \eta P^* j_{12})^2}{4 d_1 d_2}.$$

The stability or instability of the equilibrium therefore depends solely on the sign of B_{k_c}.

(i) If $d_1 j_{22} + d_2 j_{11} < 2\sqrt{d_1 d_2 \det(J)}$, then $B_{k_c} > 0$ for all $\eta \geq 0$. In this case, the second coefficient of the characteristic equation remains strictly positive, implying that no eigenvalue λ can have a positive real part. Hence, the equilibrium (N^*, P^*) is stable for all $k \geq 0$, and no Turing instability arises.

(ii) If $d_1 j_{22} + d_2 j_{11} > 2\sqrt{d_1 d_2 \det(J)}$, there exists a critical value $\eta = \eta_c^*$ such that $B_{k_c} = 0$. Solving this equality yields

$$\eta_c^* = \frac{d_1 j_{22} + d_2 j_{11} - 2\sqrt{d_1 d_2 \det(J)}}{-P^* j_{12}}.$$

Three cases are then distinguished:

- If $0 < \eta < \eta_c^*$, then $B_{k_c} < 0$, and the characteristic equation admits at least one eigenvalue with positive real part. The equilibrium becomes unstable, leading to a Turing bifurcation.
- If $\eta = \eta_c^*$, then $B_{k_c} = 0$, and the equilibrium is at the threshold of instability. The corresponding critical mode is given by

$$k_c^2 = \frac{d_1 j_{22} + d_2 j_{11} + \eta_c^* P^* j_{12}}{2 d_1 d_2},$$

which defines the stationary spatial pattern initiating the bifurcation.

- If $\eta > \eta_c^*$, then $B_{k_c} > 0$, and all eigenvalues of the characteristic equation have negative real parts. The equilibrium regains its stability, and spatial patterns disappear.

This completes the proof. □

We note that the above derivation provides a practical procedure for computing the Turing threshold. The linearized dispersion relation, together with the explicit formulas for the critical wavenumber k_c and the critical prey-taxis coefficient η_c^*, allows reproducible computation of the onset of spatial patterns and facilitates direct comparison between theoretical predictions and numerical simulations.

These results highlight the nonmonotonic role of the prey-taxis coefficient η in spatial pattern formation. When $0 < \eta < \eta_c^*$, the homogeneous equilibrium loses stability through a diffusion-driven mechanism, leading to the emergence of Turing spatial patterns. However, when η exceeds the critical threshold η_c^*, the equilibrium regains stability and the spatial patterns disappear, resulting in a homogeneous distribution of the populations.

5. Amplitude equations

The global existence and linear stability results established in the previous sections are derived in a one-dimensional bounded domain for analytical tractability. However, the weakly nonlinear analysis associated with Turing pattern selection is intrinsically a two-dimensional phenomenon.

For this reason, the derivation of amplitude equations is performed in an idealized infinite two-dimensional domain. This approach is standard in the study of Turing bifurcations and allows one to capture mode interactions responsible for stripe and hexagonal pattern selection, which cannot occur in one spatial dimension.

Although the biological habitat is a bounded domain with homogeneous Neumann boundary conditions, the weakly nonlinear analysis is performed in an idealized, infinite two-dimensional domain. This approach is standard in studies of Turing bifurcations and pattern selection mechanisms. The derivation of amplitude equations aims to describe the local behavior of the system near the critical threshold and to capture the slow modulation of the dominant unstable modes. These mechanisms depend primarily on intrinsic nonlinear interactions between critical wavenumbers, rather than boundary effects. Therefore, using an infinite domain provides a simplified analytical framework without altering the qualitative conclusions regarding pattern selection (stripes, hexagons, etc.). For sufficiently large bounded domains, the selection criteria remain valid, except for possible deformations near boundaries. This assumption should thus be interpreted as a local approximation to characterize the intrinsic mechanisms of spatial pattern formation.

The analysis of amplitude equations provides a fundamental framework for describing the dynamics of reaction–diffusion systems near the onset of a Turing bifurcation. It allows one to characterize the emergence and stability of spatial patterns such as hexagonal, stripe, or mixed spot–stripe structures, which frequently appear in ecological and biological models. To capture the slow modulation of the critical modes, we employ the multiple scale perturbation method, which is a standard technique for deriving amplitude equations in the vicinity of the bifurcation threshold.

In a two–dimensional spatial domain and near the critical value $\eta = \eta_c^*$, a hexagonal pattern can be represented as the superposition of three pairs of resonant modes $(k_j, -k_j)_{j=1,2,3}$ forming mutual angles of $2\pi/3$, with $|k_j| = k_c$ and $\sum_{j=1}^{3} k_j = 0$. Accordingly, the hexagonal solution of system (2.1) can be expressed as

$$U = U^* + \sum_{j=1}^{3}\left(A_j e^{\mathrm{i}k_j r} + \overline{A}_j e^{-\mathrm{i}k_j r}\right),$$

where A_j and $\overline{A}_j$ denote the complex amplitudes associated with the modes k_j and $-k_j$, respectively. The derivation of the amplitude equations proceeds as follows.

Step 1 - Linearization and decomposition. We introduce small perturbations around the homogeneous equilibrium by setting $N - N^* = \widetilde{N}$ and $P - P^* = \widetilde{P}$. Then, system (2.1) can be rewritten in compact form as

$$\partial_t \mathbf{U} = L\mathbf{U} + \mathbf{Q} + \mathbf{N},$$

where $\mathbf{U} = (\widetilde{N}, \widetilde{P})^T$ represents the perturbation around the equilibrium and the linear operator is $L = J_{E^*} + D\Delta$. The quadratic nonlinear term is expressed as $\mathbf{Q} = -\eta\,(0, \widetilde{P}\Delta\widetilde{N} + \nabla\widetilde{N}\cdot\nabla\widetilde{P})^T$, while the higher-order nonlinearities are given by

$$\mathbf{N} = \begin{pmatrix} \frac{1}{2}f_{20}\widetilde{N}^2 + f_{11}\widetilde{N}\widetilde{P} + \frac{1}{2}f_{02}\widetilde{P}^2 + \frac{1}{2}f_{21}\widetilde{N}^2\widetilde{P} + \frac{1}{6}f_{30}\widetilde{N}^3 + \frac{1}{2}f_{12}\widetilde{N}\widetilde{P}^2 + \frac{1}{6}f_{03}\widetilde{P}^3 + o(\varepsilon^3) \\ \frac{1}{2}g_{20}\widetilde{N}^2 + g_{11}\widetilde{N}\widetilde{P} + \frac{1}{2}g_{02}\widetilde{P}^2 + \frac{1}{2}g_{21}\widetilde{N}^2\widetilde{P} + \frac{1}{6}g_{30}\widetilde{N}^3 + \frac{1}{2}g_{12}\widetilde{N}\widetilde{P}^2 + \frac{1}{6}g_{03}\widetilde{P}^3 + o(\varepsilon^3) \end{pmatrix}.$$

where $f_{ij} = \left.\frac{\partial^{i+j}h_1}{\partial N^i \partial P^j}\right|_{(N^*,P^*)}$ and $g_{ij} = \left.\frac{\partial^{i+j}h_2}{\partial N^i \partial P^j}\right|_{(N^*,P^*)}$. Finally, the linear operator can be expressed near the critical threshold as

$$L = L^c + (\eta - \eta_c^*)\mathbf{M},$$

where

$$L^c = \begin{pmatrix} j_{11} + d_1\Delta & j_{12} \\ j_{21} - \eta_c^* P^*\Delta & j_{22} + d_2\Delta \end{pmatrix}, \qquad \mathbf{M} = \begin{pmatrix} 0 & 0 \\ -P^*\Delta & 0 \end{pmatrix}.$$

The nonlinear operator $\mathbf{Q}$ is then decomposed into a critical component evaluated at $\eta = \eta_c^*$ and a correction proportional to $(\eta - \eta_c^*)$:

$$\mathbf{Q} = \eta_c^* \begin{pmatrix} 0 \\ -\widetilde{P}\Delta\widetilde{N} - \nabla\widetilde{N}\cdot\nabla\widetilde{P} \end{pmatrix} + (\eta - \eta_c^*)\begin{pmatrix} 0 \\ -\widetilde{P}\Delta\widetilde{N} - \nabla\widetilde{N}\cdot\nabla\widetilde{P} \end{pmatrix}.$$

Step 2 — Multiple-scale expansion. To derive the amplitude equations near the critical threshold, we seek uniformly bounded solutions of order $o(\varepsilon)$ in time. Following the classical multiple-scale perturbation method, the solution of system (2.1) is expanded as

$$\mathbf{U} = \varepsilon\begin{pmatrix} N_1 \\ P_1 \end{pmatrix} + \varepsilon^2\begin{pmatrix} N_2 \\ P_2 \end{pmatrix} + \varepsilon^3\begin{pmatrix} N_3 \\ P_3 \end{pmatrix} + o(\varepsilon^3). \tag{5.1}$$

Simultaneously, the control parameter and the nonlinear term are expanded as

$$\eta_c^* - \eta = \varepsilon\eta_1 + \varepsilon^2\eta_2 + \varepsilon^3\eta_3 + o(\varepsilon^3), \qquad \mathbf{N} = \varepsilon^2\mathbf{h}_2 + \varepsilon^3\mathbf{h}_3 + o(\varepsilon^3), \tag{5.2}$$

where the quadratic and cubic nonlinearities are defined by

$$\mathbf{h}_2 = \begin{pmatrix} \frac{1}{2}f_{20}N_1^2 + f_{11}N_1P_1 + \frac{1}{2}f_{02}P_1^2 \\ \frac{1}{2}g_{20}N_1^2 + g_{11}N_1P_1 + \frac{1}{2}g_{02}P_1^2 \end{pmatrix},$$

$$\mathbf{h}_3 = \begin{pmatrix} f_{20}N_1N_2 + f_{11}(N_1P_2 + N_2P_1) + f_{02}P_1P_2 + \frac{1}{2}f_{21}N_1^2P_1 + \frac{1}{6}f_{30}N_1^3 + \frac{1}{2}f_{12}N_1P_1^2 + \frac{1}{6}f_{03}P_1^3 \\ g_{20}N_1N_2 + g_{11}(N_1P_2 + N_2P_1) + g_{02}P_1P_2 + \frac{1}{2}g_{21}N_1^2P_1 + \frac{1}{6}g_{30}N_1^3 + \frac{1}{2}g_{12}N_1P_1^2 + \frac{1}{6}g_{03}P_1^3 \end{pmatrix}.$$

To capture the slow modulation of the pattern amplitude, we introduce multiple time scales,

$$T_1 = \varepsilon t, \qquad T_2 = \varepsilon^2 t, \qquad T_3 = \varepsilon^3 t, \tag{5.3}$$

each treated as an independent variable. Consequently, the time derivative expands as

$$\frac{\partial}{\partial t} = \varepsilon\,\frac{\partial}{\partial T_1} + \varepsilon^2\,\frac{\partial}{\partial T_2} + \varepsilon^3\,\frac{\partial}{\partial T_3} + o(\varepsilon^3). \tag{5.4}$$

Substituting expansions (5.1)–(5.4) into the system (2.1) gives a hierarchy of equations at successive orders of ε.

Order $\boldsymbol{\varepsilon^1}$

$$L^c\begin{pmatrix} N_1 \\ P_1 \end{pmatrix} = \mathbf{0}. \tag{5.5}$$

Order $\boldsymbol{\varepsilon^2}$

$$L^c\begin{pmatrix} N_2 \\ P_2 \end{pmatrix} = \frac{\partial}{\partial T_1}\begin{pmatrix} N_1 \\ P_1 \end{pmatrix} + \eta_1\,\mathbf{M}\begin{pmatrix} N_1 \\ P_1 \end{pmatrix} - \eta_c^*\begin{pmatrix} 0 \\ -\nabla N_1\nabla P_1 - P_1\Delta N_1 \end{pmatrix} - \mathbf{h}_2 \;\equiv\; \mathcal{R}_2. \tag{5.6}$$

Order $\boldsymbol{\varepsilon^3}$

$$\begin{aligned} L^c\begin{pmatrix} N_3 \\ P_3 \end{pmatrix} &= \frac{\partial}{\partial T_1}\begin{pmatrix} N_2 \\ P_2 \end{pmatrix} + \frac{\partial}{\partial T_2}\begin{pmatrix} N_1 \\ P_1 \end{pmatrix} - \eta_c^*\begin{pmatrix} 0 \\ -\nabla N_1\nabla P_2 - \nabla N_2\nabla P_1 - P_1\Delta N_2 - P_2\Delta N_1 \end{pmatrix} \\ &\quad + \eta_1\,\mathbf{M}\begin{pmatrix} N_2 \\ P_2 \end{pmatrix} + \eta_2\,\mathbf{M}\begin{pmatrix} N_1 \\ P_1 \end{pmatrix} + \eta_1\begin{pmatrix} 0 \\ -\nabla N_1\nabla P_1 - P_1\Delta N_1 \end{pmatrix} - \mathbf{h}_3 \;\equiv\; \mathcal{R}_3. \end{aligned} \tag{5.7}$$

First-order solution. Since L^c is the linear operator at the critical threshold $\eta = \eta_c^*$, the vector $\binom{N_1}{P_1}$ is a linear combination of the eigenvectors associated with the zero eigenvalue. The solution of the linear problem for the critical mode ($\eta = \eta_c^*$, $|\mathbf{k}_j| = k_c$) is therefore given by

$$\begin{pmatrix} N_1 \\ P_1 \end{pmatrix} = \begin{pmatrix} \varphi \\ 1 \end{pmatrix}\left[\sum_{j=1}^{3} U_j\, e^{\mathrm{i}\mathbf{k}_j\cdot\mathbf{r}}\right] + \text{c.c.}, \tag{5.8}$$

where

$$\varphi = \frac{j_{12}}{d_1k_c^2 - j_{11}}, \qquad |\mathbf{k}_j| = k_c,$$

and U_j denotes the amplitude of the mode $e^{\mathrm{i}\mathbf{k}_j\cdot\mathbf{r}}$ ($j = 1, 2, 3$) at first order. Here, $\mathbf{r} = (x, y)$ is the spatial variable in two dimensions, and "c.c." stands for the complex conjugate of the preceding terms.

Fredholm solvability condition (second order). To ensure the existence of nontrivial solutions to the second-order system, the Fredholm solvability condition requires that $\mathcal{R}_2$ be orthogonal to the null eigenvectors of the adjoint operator $\mathcal{L}_c^*$. These adjoint eigenvectors are expressed as

$$\begin{pmatrix} 1 \\ \psi \end{pmatrix} e^{-\mathrm{i}\mathbf{k}_j\cdot\mathbf{r}} + \text{c.c.}, \qquad j = 1, 2, 3, \tag{5.9}$$

where

$$\psi = \frac{d_1 k_c^2 - j_{11}}{j_{21} + \eta_c^* P^* k_c^2}.$$

If we denote by $\mathcal{R}_2^j$ the coefficient associated with $e^{\mathrm{i}\mathbf{k}_j\cdot\mathbf{r}}$ in $\mathcal{R}_2$, the Fredholm condition implies

$$(1, \psi)\,\mathcal{R}_2^j = 0, \qquad j = 1, 2, 3. \tag{5.10}$$

Amplitude equations at order ε^1. Applying the above solvability condition yields the system governing the evolution of the complex amplitudes U_j $(j = 1, 2, 3)$:

$$\begin{cases} (\varphi + \psi)\,\dfrac{\partial U_1}{\partial T_1} = -\,\eta_1 k_c^2 P^*\, U_1 + (l + \psi\,\eta_c^* k_c^2 \varphi + \psi\, m)\,\overline{U}_2\,\overline{U}_3, \\ (\varphi + \psi)\,\dfrac{\partial U_2}{\partial T_1} = -\,\eta_1 k_c^2 P^*\, U_2 + (l + \psi\,\eta_c^* k_c^2 \varphi + \psi\, m)\,\overline{U}_3\,\overline{U}_1, \\ (\varphi + \psi)\,\dfrac{\partial U_3}{\partial T_1} = -\,\eta_1 k_c^2 P^*\, U_3 + (l + \psi\,\eta_c^* k_c^2 \varphi + \psi\, m)\,\overline{U}_1\,\overline{U}_2, \end{cases} \tag{5.11}$$

where $l = f_{20}\varphi^2 + 2f_{11}\varphi + f_{02}$ and $m = g_{20}\varphi^2 + 2g_{11}\varphi + g_{02}$.

Second-order expansion. At the second order in ε, the correction term $\mathbf{U}_2 = (N_2, P_2)^T$ can be expressed as a superposition of resonant and nonresonant modes arising from the quadratic interactions of the critical modes. Specifically, we write

$$\begin{aligned} \begin{pmatrix} N_2 \\ P_2 \end{pmatrix} = \begin{pmatrix} U_0 \\ V_0 \end{pmatrix} + \sum_{j=1}^{3} \begin{pmatrix} U_j \\ V_j \end{pmatrix} e^{\mathrm{i}\mathbf{k}_j\cdot\mathbf{r}} + \sum_{j=1}^{3} \begin{pmatrix} U_{jj} \\ V_{jj} \end{pmatrix} e^{2\mathrm{i}\mathbf{k}_j\cdot\mathbf{r}} \\ + \begin{pmatrix} U_{12} \\ V_{12} \end{pmatrix} e^{\mathrm{i}(\mathbf{k}_1-\mathbf{k}_2)\cdot\mathbf{r}} + \begin{pmatrix} U_{23} \\ V_{23} \end{pmatrix} e^{\mathrm{i}(\mathbf{k}_2-\mathbf{k}_3)\cdot\mathbf{r}} + \begin{pmatrix} U_{31} \\ V_{31} \end{pmatrix} e^{\mathrm{i}(\mathbf{k}_3-\mathbf{k}_1)\cdot\mathbf{r}} + \text{c.c.} \end{aligned} \tag{5.12}$$

The above representation takes into account the zero mode (e^0), the fundamental modes ($e^{\mathrm{i}\mathbf{k}_j\cdot\mathbf{r}}$), the second harmonics ($e^{2\mathrm{i}\mathbf{k}_j\cdot\mathbf{r}}$), and the difference modes ($e^{\mathrm{i}(\mathbf{k}_j-\mathbf{k}_\ell)\cdot\mathbf{r}}$) generated by the nonlinear coupling of the critical wavevectors.

By substituting (5.12) and the first-order expansion (5.8) into the governing relation (5.6), and equating the coefficients of these harmonics, we obtain the following solvability conditions for each spatial contribution:

$$\begin{pmatrix} U_0 \\ P_0 \end{pmatrix} = \begin{pmatrix} N_{00} \\ P_{00} \end{pmatrix} (|U_1|^2 + |U_2|^2 + |U_3|^2), \qquad U_j = \varphi\, V_j. \tag{5.13}$$

The second-harmonic and mixed-mode components satisfy

$$\begin{pmatrix}U_{jj}\\V_{jj}\end{pmatrix}=\begin{pmatrix}N_{11}\\P_{11}\end{pmatrix}U_j^2,\qquad \begin{pmatrix}U_{j\ell}\\V_{j\ell}\end{pmatrix}=\begin{pmatrix}N_\star\\P_\star\end{pmatrix}U_j\,\overline{U}_\ell,\qquad j,\ell\in\{1,2,3\},\ j\neq\ell. \tag{5.14}$$

The corresponding coefficients are then given by

$$\begin{pmatrix}N_{00}\\P_{00}\end{pmatrix}=\begin{pmatrix}\dfrac{-\,j_{22}\,l+j_{12}\,m}{j_{11}j_{22}-j_{12}j_{21}}\\[2mm]\dfrac{-\,j_{11}\,m+j_{21}\,l}{j_{11}j_{22}-j_{12}j_{21}}\end{pmatrix}, \tag{5.15}$$

$$\begin{pmatrix}N_{11}\\P_{11}\end{pmatrix}=\begin{pmatrix}\dfrac{-\frac{l}{2}(j_{22}-4d_2k_c^2)+\frac{m}{2}j_{12}+2\eta_c^*\varphi k_c^2j_{12}}{(j_{11}-4d_1k_c^2)(j_{22}-4d_2k_c^2)-j_{12}(j_{21}+4\eta_c^*P^*k_c^2)}\\[2mm]\dfrac{-\frac{m}{2}(j_{11}-4d_1k_c^2)-2\eta_c^*\varphi k_c^2(j_{11}-4d_1k_c^2)+\frac{l}{2}(j_{21}+4\eta_c^*P^*k_c^2)}{(j_{11}-4d_1k_c^2)(j_{22}-4d_2k_c^2)-j_{12}(j_{21}+4\eta_c^*P^*k_c^2)}\end{pmatrix}, \tag{5.16}$$

and

$$\begin{pmatrix}N_\star\\P_\star\end{pmatrix}=\begin{pmatrix}\dfrac{-\,l\,(j_{22}-3d_2k_c^2)+(m+3\,\eta_c^*\varphi k_c^2)\,j_{12}}{(j_{11}-3d_1k_c^2)(j_{22}-3d_2k_c^2)-j_{12}(j_{21}+3\,\eta_c^*P^*k_c^2)}\\[2mm]\dfrac{-(m+3\,\eta_c^*\varphi k_c^2)(j_{11}-3d_1k_c^2)+l\,(j_{21}+3\,\eta_c^*P^*k_c^2)}{(j_{11}-3d_1k_c^2)(j_{22}-3d_2k_c^2)-j_{12}(j_{21}+3\,\eta_c^*P^*k_c^2)}\end{pmatrix}. \tag{5.17}$$

Third-order expansion. At the third order in ε, substituting the previous expansions into $\mathcal{R}_3$ and collecting the coefficients of $\exp(\mathrm{i}\mathbf{k}_j\cdot\mathbf{r})$ for $j=1,2,3$, we define $(R_u^j,R_v^j)^\mathsf{T}$ as the corresponding components of $\mathcal{R}_3$. The resulting expressions read

$$\begin{pmatrix}R_u^1\\R_v^1\end{pmatrix}=\begin{pmatrix}\varphi\\1\end{pmatrix}\left(\frac{\partial V_1}{\partial T_1}+\frac{\partial W_1}{\partial T_2}\right)+\begin{pmatrix}0\\\eta_1N_*k_c^2\end{pmatrix}V_1+\begin{pmatrix}0\\\eta_2N_*k_c^2\end{pmatrix}W_1+\begin{pmatrix}0\\3\eta_1k_c^2\varphi\end{pmatrix}\overline{W}_2\overline{W}_3$$

$$+\begin{pmatrix}I_1\\J_1\end{pmatrix}|W_1|^2W_1+\begin{pmatrix}I_2\\J_2\end{pmatrix}(|W_2|^2+|W_3|^2)W_1-\begin{pmatrix}l\\m+\eta_c^*k_c^2\varphi\end{pmatrix}(\overline{W}_2\overline{V}_3+\overline{W}_3\overline{V}_2).$$

The coefficients I_i and J_i are given by

$$\begin{aligned}I_1&=-(N_{11}+N_{00})(\varphi b_{20}+b_{11})-(\varphi b_{11}+b_{02})(P_{11}+P_{00})-\left(\tfrac{b_{30}\varphi^3}{2}+\tfrac{b_{03}}{2}\right)\\&\quad-\left(\tfrac{3}{2}b_{21}\varphi^2+\tfrac{3}{2}b_{12}\varphi\right),\end{aligned}$$

$$\begin{aligned}I_2&=-(N_*+N_{00})(\varphi b_{20}+b_{11})-(\varphi b_{11}+b_{02})(P_*+P_{00})-(b_{30}\varphi^3+b_{03})\\&\quad-(3b_{21}\varphi^2+3b_{12}\varphi),\end{aligned}$$

$$J_1=-(N_{11}+N_{00})(\varphi c_{20}+c_{11})-(\varphi c_{11}+c_{02})(P_{11}+P_{00})-\left(\tfrac{c_{30}\varphi^3}{2}+\tfrac{c_{03}}{2}\right)$$

$$- \left(\tfrac{3}{2}c_{21}\varphi^2 + \tfrac{3}{2}c_{12}\varphi\right) - 2k_c^2\varphi\eta_c^* P_{11} + k_c^2\eta_c^* N_{11},$$

$$\begin{aligned} J_2 = & -(N_* + N_{00})(\varphi c_{20} + c_{11}) - (\varphi c_{11} + c_{02})(P_* + P_{00}) - (c_{30}\varphi^3 + c_{03}) \\ & - (3c_{21}\varphi^2 + 3c_{12}\varphi) - \tfrac{3}{2}\eta_c^* k_c^2 \varphi P_* + \tfrac{1}{2}\eta_c^* k_c^2 N_*. \end{aligned}$$

The corresponding terms $(R_u^2, R_v^2)^\top$ and $(R_u^3, R_v^3)^\top$ can be obtained by cyclic permutation of the indices of U and V. The Fredholm solvability condition requires that the inhomogeneous term $(R_u^1, R_v^1)^\top$ be orthogonal to the null eigenvectors of the adjoint operator $\mathcal{L}_c^*$. Consequently, one obtains

$$\begin{cases} (\varphi + \psi)\left(\frac{\partial V_1}{\partial T_1} + \frac{\partial U_1}{\partial T_2}\right) = k_c^2 N_*(\chi_1 V_1 + \chi_2 U_1) + 3\eta_1 k_c^2 \varphi \overline{U}_2 \overline{U}_3 \\ \qquad + (l + \eta_s k_c^2 \varphi + \psi m)(\overline{U}_2 \overline{V}_3 + \overline{U}_3 \overline{V}_2) - [G_1 |U_1|^2 + G_2(|U_2|^2 + |U_3|^2)]U_1, \\ (\varphi + \psi)\left(\frac{\partial V_2}{\partial T_1} + \frac{\partial U_2}{\partial T_2}\right) = k_c^2 N_*(\chi_1 V_2 + \chi_2 U_2) + 3\eta_1 k_c^2 \varphi \overline{U}_3 \overline{U}_1 \\ \qquad + (l + \eta_s k_c^2 \varphi + \psi m)(\overline{U}_3 \overline{V}_1 + \overline{U}_1 \overline{V}_3) - [G_1 |U_2|^2 + G_2(|U_3|^2 + |U_1|^2)]U_2, \\ (\varphi + \psi)\left(\frac{\partial V_3}{\partial T_1} + \frac{\partial U_3}{\partial T_2}\right) = k_c^2 N_*(\chi_1 V_3 + \chi_2 U_3) + 3\eta_1 k_c^2 \varphi \overline{U}_1 \overline{U}_2 \\ \qquad + (l + \eta_s k_c^2 \varphi + \psi m)(\overline{U}_1 \overline{V}_2 + \overline{U}_2 \overline{V}_1) - [G_1 |U_3|^2 + G_2(|U_1|^2 + |U_2|^2)]U_3, \end{cases} \tag{5.18}$$

where $G_1 = I_1 + \psi J_1$ and $G_2 = I_2 + \psi J_2$.

Step 3. Derivation of the amplitude equations. At this stage, the amplitude functions A_j are introduced to capture the slow modulation of the critical modes near the bifurcation threshold. From Eq (5.4), their evolution satisfies

$$\frac{\partial A_j}{\partial t} = \varepsilon \frac{\partial A_j}{\partial T_1} + \varepsilon^2 \frac{\partial A_j}{\partial T_2} + \cdots, \tag{5.19}$$

and we expand

$$A_j = \varepsilon\, U_j + \varepsilon^2\, V_j + o(\varepsilon^3). \tag{5.20}$$

By substituting expansions (5.19) and (5.20) together with the results obtained in the previous steps, we derive the coupled amplitude equations governing the temporal evolution of the three interacting modes:

$$\begin{cases} \tau_0 \dfrac{\partial A_1}{\partial t} = \mu A_1 + \kappa \overline{A}_2 \overline{A}_3 - [g_1 |A_1|^2 + g_2(|A_2|^2 + |A_3|^2)]A_1, \\ \tau_0 \dfrac{\partial A_2}{\partial t} = \mu A_2 + \kappa \overline{A}_1 \overline{A}_3 - [g_1 |A_2|^2 + g_2(|A_1|^2 + |A_3|^2)]A_2, \\ \tau_0 \dfrac{\partial A_3}{\partial t} = \mu A_3 + \kappa \overline{A}_1 \overline{A}_2 - [g_1 |A_3|^2 + g_2(|A_1|^2 + |A_2|^2)]A_3. \end{cases} \tag{5.21}$$

The coefficients involved are given by

$$\tau_0 = \frac{\varphi + \psi}{-\eta_s^c\, k_c^2 N_*}, \qquad \mu = \frac{\eta_s^c - \eta}{\eta_s^c}, \qquad g_1 = \frac{G_1}{-\eta_s^c\, k_c^2 N_*}, \qquad g_2 = \frac{G_2}{-\eta_s^c\, k_c^2 N_*},$$

$$\kappa = -\frac{l + \eta_s k_c^2 \varphi + \psi m}{\eta_s^c k_c^2 N_*} - \frac{3\varphi\mu}{N_*}.$$

Remark. The expression of κ clearly shows that the predator-taxis coefficient χ strongly affects the quadratic term in the amplitude system (5.21), thereby influencing pattern selection near the critical threshold.

Linear stability analysis of the amplitude system. We next perform a linear stability analysis of system (5.21). Let

$$A_j = \rho_j e^{\mathrm{i}\theta_j}, \qquad j = 1, 2, 3, \tag{5.22}$$

where ρ_j and θ_j denote, respectively, the modulus and the phase of each amplitude. Substituting (5.22) into (5.21) and separating the real and imaginary parts yield

$$\begin{cases} \tau_0 \dfrac{\partial \theta}{\partial t} = -\kappa \dfrac{\rho_1^2\rho_2^2 + \rho_1^2\rho_3^2 + \rho_2^2\rho_3^2}{\rho_1\rho_2\rho_3} \sin\theta, \\ \tau_0 \dfrac{\partial \rho_1}{\partial t} = \mu\rho_1 + \kappa\rho_2\rho_3 \cos\theta - g_1\rho_1^3 - g_2(\rho_2^2 + \rho_3^2)\rho_1, \\ \tau_0 \dfrac{\partial \rho_2}{\partial t} = \mu\rho_2 + \kappa\rho_1\rho_3 \cos\theta - g_1\rho_2^3 - g_2(\rho_1^2 + \rho_3^2)\rho_2, \\ \tau_0 \dfrac{\partial \rho_3}{\partial t} = \mu\rho_3 + \kappa\rho_1\rho_2 \cos\theta - g_1\rho_3^3 - g_2(\rho_1^2 + \rho_2^2)\rho_3, \end{cases} \tag{5.23}$$

where $\theta = \theta_1 + \theta_2 + \theta_3$.

Stationary states and pattern selection. At equilibrium, θ satisfies $\theta = 0$ or $\theta = \pi$. Substituting these conditions into (5.23) yields

$$\begin{cases} \tau_0 \dfrac{\partial \rho_1}{\partial t} = \mu\rho_1 + |\kappa|\rho_2\rho_3 - g_1\rho_1^3 - g_2(\rho_2^2 + \rho_3^2)\rho_1, \\ \tau_0 \dfrac{\partial \rho_2}{\partial t} = \mu\rho_2 + |\kappa|\rho_1\rho_3 - g_1\rho_2^3 - g_2(\rho_1^2 + \rho_3^2)\rho_2, \\ \tau_0 \dfrac{\partial \rho_3}{\partial t} = \mu\rho_3 + |\kappa|\rho_1\rho_2 - g_1\rho_3^3 - g_2(\rho_1^2 + \rho_2^2)\rho_3. \end{cases} \tag{5.24}$$

Clearly, $\mu > 0$ when $\chi < \chi_s^c$, and $|\kappa| > 0$ always holds. For stationary solutions to exist, the coefficients g_1 and g_2 must be positive. Under these conditions, system (5.24) admits the following steady states:

- *Homogeneous steady state (HSS):* $\rho_1 = \rho_2 = \rho_3 = 0$.
- *Stripe pattern (S):* $\rho_1 = \pm\sqrt{\frac{\mu}{g_1}} \neq 0, \quad \rho_2 = \rho_3 = 0$.
- *Hexagonal patterns H_0 and H_π:* for $\theta = 0$ or π, respectively,

$$\rho_1 = \rho_2 = \rho_3 = \frac{|\kappa|}{2(g_1 + 2g_2)} \pm \sqrt{\frac{\mu}{g_1 + 2g_2}},$$

which exist whenever $\mu > -\frac{\kappa^2}{4(g_1+2g_2)}$.

Introducing

$$\nu = \frac{\mu}{\kappa^2}, \qquad \nu_1 = -\frac{1}{4(g_1 + 2g_2)}, \quad \nu_2 = 0, \quad \nu_3 = \frac{g_1}{(g_2 - g_1)^2}, \quad \nu_4 = \frac{2g_1 + g_2}{(g_2 - g_1)^2}, \tag{5.25}$$

we observe that $\nu_1 < \nu_2 < \nu_3 < \nu_4$, which leads to the following theorem on pattern selection.

Theorem 4. *Assume that $g_1, g_2 > 0$. The stability and bifurcation behavior depend on the relative magnitude of these coefficients as follows.*

***(i) Case** $g_1 < g_2$.*

1) The homogeneous steady state (HSS) is stable for $\nu < \nu_2$ and becomes unstable for $\nu > \nu_2$.

2) Hexagonal patterns exist for $\nu > \nu_1$.

- *If $\kappa > 0$, the H_0 branch is stable when $\nu < \nu_4$ and unstable for $\nu > \nu_4$, while H_π remains unstable.*
- *If $\kappa < 0$, the opposite occurs: H_π is stable for $\nu < \nu_4$ and unstable for $\nu > \nu_4$, whereas H_0 is always unstable.*

3) The stripe (or roll) pattern S is stable for $\nu > \nu_3$ and unstable for $\nu < \nu_3$.

***(ii) Case** $g_1 > g_2$.*

1) The homogeneous steady state remains stable for $\nu < \nu_2$ and loses stability for $\nu > \nu_2$.

2) Hexagonal solutions H_0 and H_π exist for $\nu > \nu_1$.

- *For $\kappa > 0$, H_0 is stable when $\nu < \nu_4$ and unstable otherwise, while H_π is always unstable.*
- *For $\kappa < 0$, H_π is stable for $\nu < \nu_4$ and unstable for $\nu > \nu_4$, whereas H_0 remains unstable.*

3) The stripe pattern is always unstable regardless of the value of ν.

6. Numerical simulations

This section focuses on the numerical study of the spatiotemporal predator-prey model. We describe the methodology used to solve it and present results aimed at validating our theoretical conclusions regarding the emergence of spatial structures.

While the analytical results presented in the previous sections are derived in a one-dimensional spatial domain for mathematical tractability, the numerical simulations are extended to two- and three-dimensional domains. These higher-dimensional computations are intended to illustrate the richness of possible spatial organizations and to visualize pattern structures that cannot arise in one dimension.

The main objective of our simulations is to confirm the validity of Turing's instability conditions and to highlight the stable nonconstant stationary states that form when the system crosses the bifurcation threshold from the homogeneous state. We will seek to characterize these spatial patterns not only in classical one-dimensional (1D) and two-dimensional (2D) domains, but also on more complex geometries such as spherical and cubic surfaces, to assess the influence of topology on morphogenesis.

6.1. Parameters, local stability, and resolution method

The numerical simulations were performed using the Matlab computing environment. The spatiotemporal integration of system (2.1) was carried out by employing a finite difference scheme to discretize the equations. The numerical values of the parameters used for these simulations are selected to satisfy the conditions for pattern emergence and are grouped in Table 2.

Table 2. Numerical values of the ecological and behavioral parameters used for the simulations.

α	β	γ	m_1	δ	a	b	c	μ_1	μ_2	E_1	E_2	ε	m_2
1.5	0.01	0.8	0.8	0.1	0.6	0.09	0.04	0.05	0.02	0.056	0.045	0.5	0.2

With these parameter values, the calculation of the associated stationary system leads to the unique nontrivial positive equilibrium point $(N^*, P^*) = (0.97,\ 0.32)$. This homogeneous state is used as the basis for initializing the spatiotemporal simulation by introducing a small random perturbation to initiate the pattern formation process.

6.2. Validation of homogeneous state stability

Before activating the diffusion and taxis terms, we confirm the stability of the equilibrium state (N^*, P^*) in the associated ordinary dynamic system (ODS, i.e., system (2.1) with $d_1 = d_2 = \eta = 0$). The stability of the nonspatial system is first established analytically by applying the Routh-Hurwitz criterion to the characteristic polynomial of the Jacobian matrix, which confirms that all eigenvalues have negative real parts. This theoretical finding is validated through time-series simulations: Figures 1 and 2 graphically illustrate that any trajectory initiated near (N^*, P^*) quickly converges to this equilibrium point. This demonstrates that the equilibrium state is locally asymptotically stable in the absence of spatial components (diffusion and taxis), consistent with Lyapunov's second method.

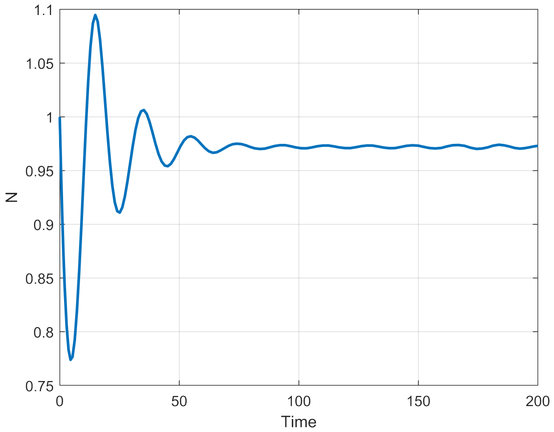

Figure 1. Phase portrait of the prey population N around the interior equilibrium point $(N^*, P^*) = (0.97, 0.32)$. The horizontal axis represents the prey density N, and the vertical axis represents its rate of change $\dot{N}$. Trajectories initialized near the equilibrium converge to (N^*, P^*), confirming local asymptotic stability in the absence of spatial effects.

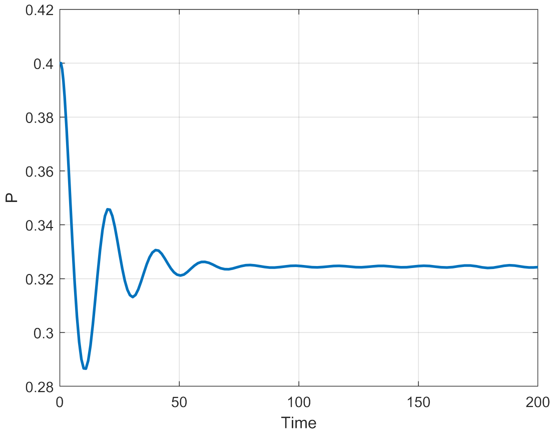

Figure 2. Phase portrait of the predator population P around the interior equilibrium $(N^*, P^*) = (0.97, 0.32)$. The horizontal axis shows predator density P, and the vertical axis its rate of change $\dot{P}$. Trajectories starting near the equilibrium point converge to (N^*, P^*), illustrating the stability of the predator dynamics without diffusion or taxis.

6.3. *Bifurcation analysis and pattern selection*

To further clarify the role of the prey–taxis coefficient, Figure 3 illustrates the regime map with respect to η. The diagram summarizes the theoretical prediction that spatial patterns occur when $0 < \eta < \eta_c^*$, while the homogeneous equilibrium becomes stable for $\eta > \eta_c^*$. The critical threshold is $\eta_c^* = 0.985$.

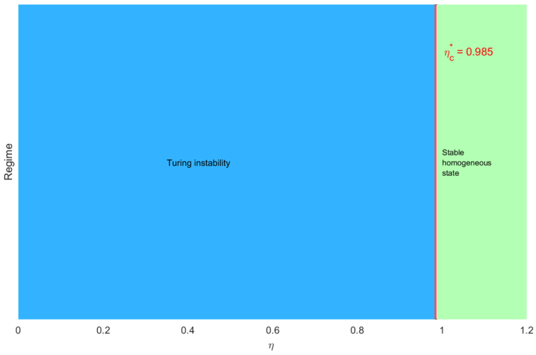

Figure 3. Regime map illustrating the influence of the prey–taxis coefficient η on the system dynamics.

In Figure 4, we illustrate the hexagonal pattern selection. First, we consider the parameter sets $\alpha = 1.5, \beta = 0.01, \gamma = 0.8, m_1 = 0.8, \delta = 0.1, a = 0.6, b = 0.09, c = 0.04, \mu_1 = 0.05, \mu_2 = 0.02, E_1 = 0.056, E_2 = 0.045, \varepsilon = 0.5$, and $m_2 = 0.2$. Then from the linear stability analysis, we find the corresponding prey-taxis Turing threshold $\eta_c^* = 0.985$. Note that the system (2.1) has Turing instability for $\eta < \eta_c^*$. From the weakly nonlinear analysis, we obtain $g_2 = 0.8 > g_1 = 0.3 > 0$ and $\kappa = 0.8$. Further, we obtain $\nu_1 = -0.0064$, $\nu_2 = 0$, $\nu_3 = 0.12$, and $\nu_4 = 0.2917$. According to the Theorem 5.1, we have shown a pattern selection bifurcation diagram (see Figure 4), which concludes that hexagon patterns appear in the range (ν_1, ν_3), mixture of hexagons and stripe patterns appear in the range (ν_3, ν_4), and stripe patterns appear for $\nu > \nu_4$. If we consider prey-taxis coefficient $\eta = 0.6 < \eta_c^*$, then $\nu = (\eta_c^* - \eta)/\eta_c^* = 0.1241 \in (\nu_3, \nu_4)$.

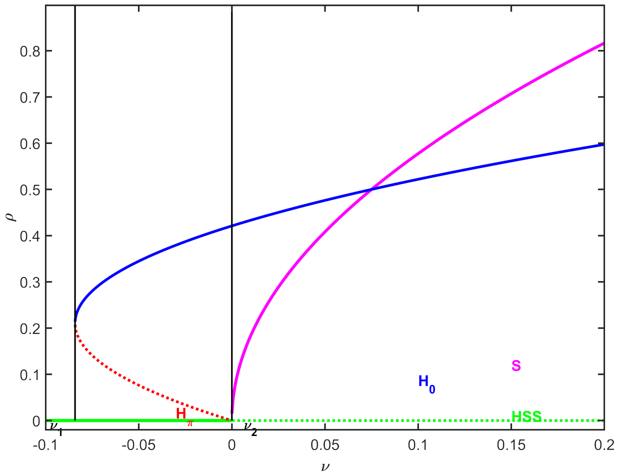

Figure 4. Hexagonal pattern selection bifurcation diagram. Here the dotted and solid curves represent the corresponding unstable and stable steady-state solutions, respectively.

This theoretical bifurcation analysis provides crucial insights for understanding the pattern selection observed in our subsequent numerical simulations.

6.4. Impact of the parameters β, ε, and γ on the system dynamics

The dynamics of the predator-prey system are profoundly influenced by its key parameters, as illustrated in Figures 5(a),(b), 6–8.

To better understand the impact of critical parameters on species density, we use contour plots to visualize this relationship (see Figure 5(a),(b)). These plots effectively illustrate how the densities of different populations in the system evolve when two key parameters, the Allee threshold β and the conversion efficiency ε, vary simultaneously. Figure 5(a) clearly illustrates that an increase in the Allee effect parameter β results in a drastic reduction in the prey population density, eventually leading it to extinction (transition from red/yellow to deep blue). This abrupt collapse reflects a saddle-node bifurcation, highlighting β as the main factor determining prey persistence. Conversely, in the stable coexistence region (low β), a higher conversion efficiency ε results in a decrease in prey density, with the most efficient predator exerting stronger top-down control.

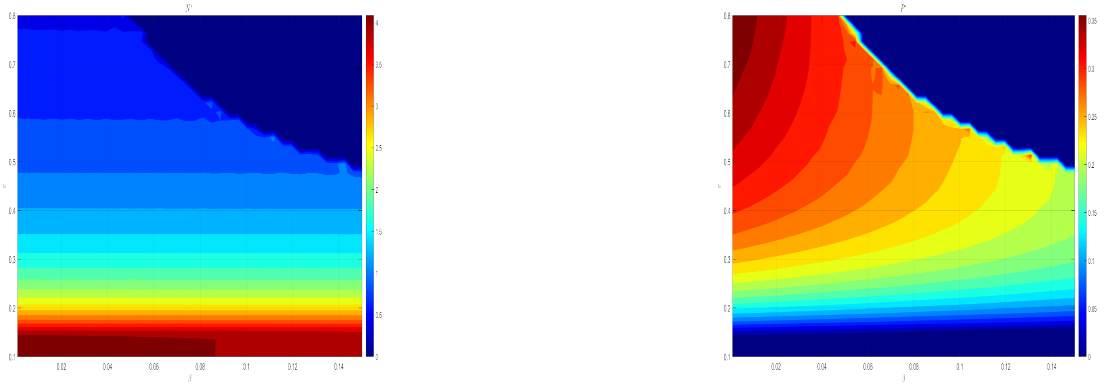

(a) (b)

Figure 5. Contour plots representing the equilibrium densities of the prey and predator population as a function of β and ε. The parameters are taken with the same values as in Table 2.

Examining Figure 5(b) sheds further light on these dynamics: A robust predator population (red/yellow regions) is only maintained when the prey population is viable (i.e., when β is low). Increasing ε generally increases predator density in the coexistence zone, reflecting enhanced energy transfer. However, beyond a critical Allee threshold, the predator population inevitably collapses to zero, reflecting prey extinction, demonstrating its direct dependence. Therefore, examining species density through these contour lines is crucial to understanding the complex interplay of parameters and their profound effects on long-term ecosystem stability and species coexistence, particularly with respect to the vulnerability introduced by the Allee effect and the balance of trophic efficiency.

Figure 6 explores the combined effect of β and ε on the global dynamics and stability of the predator–prey system. The figure shows a bifurcation surface or contour map, where distinct regions correspond to coexistence, oscillatory behavior, or extinction. Stable coexistence is observed when β remains small (weak Allee effect) and ε takes moderate values. In contrast, large β values combined with high ε lead to extinction of the prey, and eventually the predator, due to insufficient reproductive capacity under intense predation. Conversely, when ε is too small, predators cannot persist even if prey survive. The interplay between these parameters thus determines the system's resilience, revealing that the balance between prey reproductive ability and predator energetic efficiency is crucial for maintaining long-term coexistence.

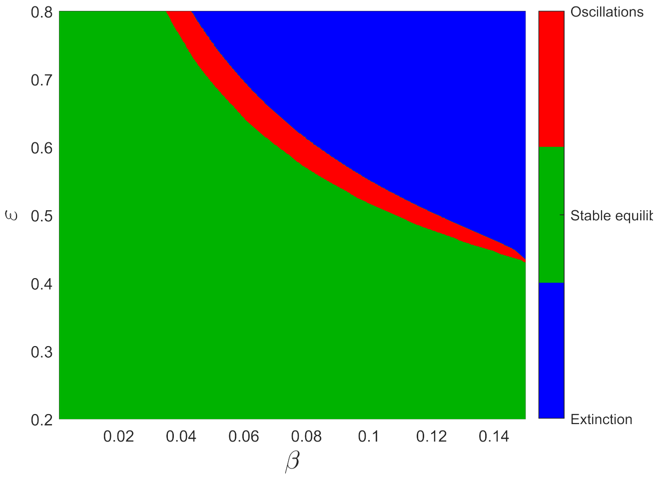

Figure 6. Interaction between β and ε parameters in shaping predator–prey dynamics.

In Figure 7(a), the effect of the conversion efficiency ε, which quantifies the predator's ability to transform consumed prey biomass into its own growth, is analyzed. For low ε values, predators utilize prey resources inefficiently, maintaining low abundance while the prey population remains stable and dense. As ε increases, the predator population grows and prey density decreases, showing stronger predation pressure and energy transfer. However, beyond a certain efficiency level, the system can become unstable, potentially leading to oscillations or collapse. This highlights the delicate energetic balance required for stable coexistence, as excessive predator efficiency can destabilize the ecosystem through overexploitation.

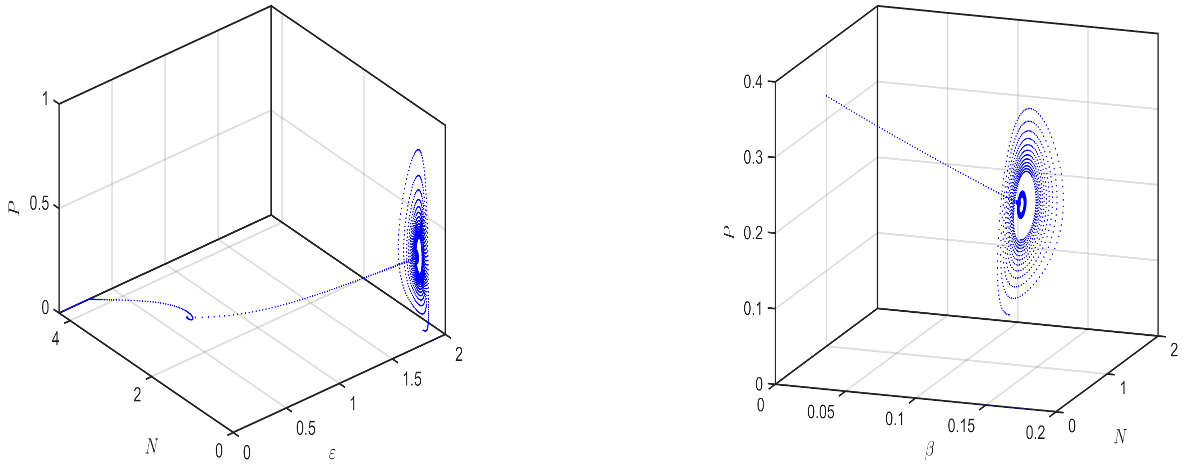

(a)

(b)

Figure 7. Impact of the conversion efficiency (ε) (a) and the Allee threshold (β) (b) on predator–prey dynamics. The contour plots illustrate how variations in these parameters affect the equilibrium densities of prey and predator populations.

As shown in Figure 7(b), increasing the Allee parameter β significantly alters the prey population's persistence capacity. For low β values ($\beta = 0$ and 0.05), the prey population maintains a high and stable equilibrium, indicating efficient reproduction even at low densities. When β increases to 0.10 and 0.15, the prey density gradually decreases, reflecting the growing reproductive difficulty at low population sizes. At $\beta = 0.20$, the system exhibits a near-collapse of the prey population, indicating that the Allee effect becomes dominant and strongly limits recovery. This behavior represents the approach of a saddle-node bifurcation, where the prey's equilibrium density drops sharply as β increases, revealing the sensitivity of prey survival to low-density effects. Ecologically, it demonstrates that even a moderate rise in the Allee threshold can drive the prey toward extinction if its density falls below a critical reproductive level.

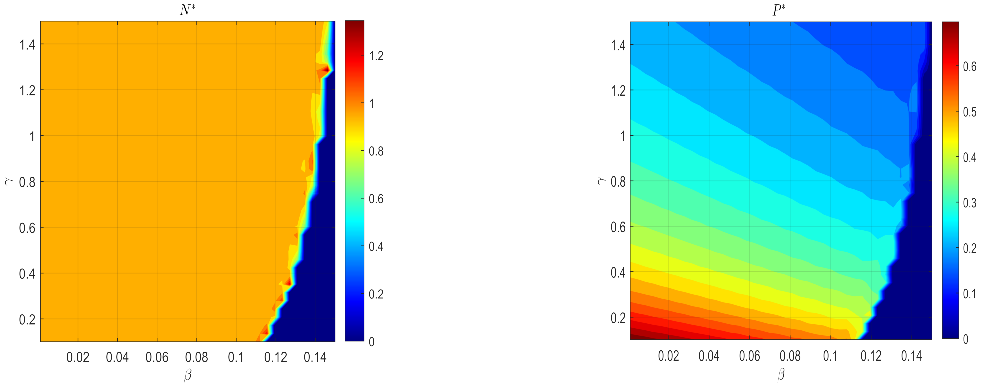

(a) (b)

Figure 8. Contour plots representing the equilibrium densities of the prey and predator population as a function of β and γ. The parameters are taken with the same values as in Table 2.

The contour plot (Figure 8(a)), representing the equilibrium density of the prey population (N^*) as a function of the Allee threshold and the fear intensity, vividly illustrates the combined pressures of an intrinsic demographic bottleneck and a behavioral stressor. The region of highest prey density (warm colors) is strictly confined to the lower-left corner, demanding both a minimal Allee effect ($\beta \approx 0$) and a minimal fear response ($\gamma \approx 0$). Moving horizontally, the increase in the Allee threshold (β) acts as the primary extinction driver, causing an abrupt collapse of N^* to zero across all levels of fear. This confirms that the demographic constraint imposed by β is a nonnegotiable boundary, signifying a saddle-node bifurcation. Conversely, moving vertically, the increase in fear intensity (γ) leads to a monotonic and gradual reduction in N^* within the viable zone. This decline is due to the prey's reduced per capita growth rate ($\frac{1}{1+\gamma P}$), as time spent avoiding predators compromises feeding and reproduction, effectively lowering the ecosystem's carrying capacity for the prey. Consequently, the two factors operate synergistically: The Allee effect (β) sets the survival boundary, while the fear effect (γ) steadily erodes the maximum achievable population size within that boundary, making the prey increasingly vulnerable to demographic and environmental fluctuations.

The Figure 8(b) illustrates the equilibrium density of the predator population (P^*) as a function of the Allee threshold (β) and fear intensity (γ). It reveals how these two ecological constraints, one demographic (Allee), the other behavioral (fear), jointly define the predator's viability.

The graph shows that the region of high predator density (warm colors, yellow and red) is confined to a parameter window where the Allee threshold is low (β close to zero). The most drastic impact is exerted by β: When it exceeds a critical threshold (around $\beta \approx 0.15$), the predator population abruptly collapses towards zero, forming a vertical extinction boundary (transition to dark blue). This behavior is a direct consequence of prey extinction caused by exceeding the Allee threshold, confirming that β is the ultimate limiting factor for the persistence of the entire ecosystem.

Fear intensity (γ), varying vertically, modulates predator density within the viable coexistence zone. Increasing γ (upward movement) results in a progressive reduction of P^* (transition from red to yellow to green). This decline is explained by the fact that increased fear in the prey (N) reduces its effective reproductive rate and, consequently, its equilibrium density, which inevitably limits the amount of resources available to the predator. In summary, the Allee threshold defines the predator's survival boundary, while fear intensity regulates its maximum achievable density within this boundary. The highest predator density is reached in the lower left corner, where both constraints are minimal.

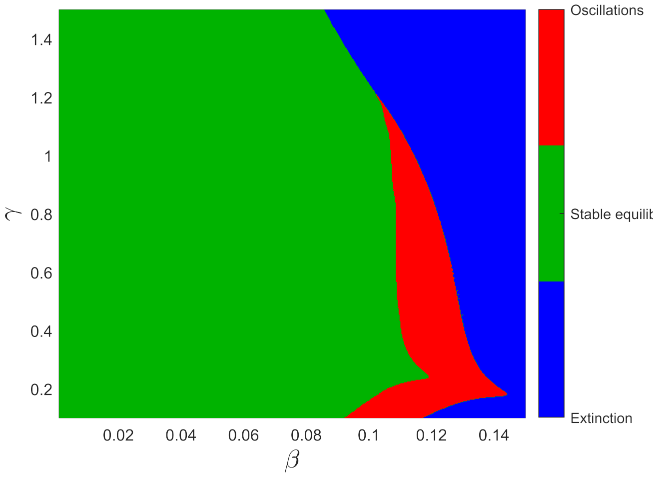

Figure 9. Interaction between β and γ parameters in shaping predator–prey dynamics.

Figure 9 represents a two-parameter bifurcation diagram, plotted in the plane of the Allee threshold β and fear intensity γ, which maps the fundamental dynamical domains of the predator-prey system, revealing three distinct regions governed by two critical curves: the Hopf bifurcation curve (H), which separates stable coexistence from sustained oscillations (limit cycles), and the saddle-node bifurcation curve (SN), which marks the threshold of irreversible extinction. The evolution of the system is primarily dictated by the Allee threshold β: For low values of β, the system maintains a stable equilibrium; however, a slight increase in β beyond the H curve destabilizes the equilibrium, leading to potentially harmful oscillations for the ecosystem. If β continues to increase and crosses the SN curve, the positive equilibrium disappears entirely, inevitably leading to the extinction of both species. The fear intensity γ very slightly modulates the position of these boundaries, indicating that, although fear significantly affects population density (as observed in previous contour figures), it plays a secondary role compared to the Allee effect in determining the type of stability and the ultimate fate of the system. This diagram thus demonstrates that effective management must keep β well below the Hopf curve to ensure stable coexistence without the risk of damaging oscillations or a complete demographic collapse. The results highlight that the Allee effect (β) acts as a primary extinction driver, whereas fear intensity (γ) modulates population densities within the viable range. In a marine ecosystem context, this implies that populations with low-density reproductive constraints are highly sensitive to perturbations, and even moderate stressors can push prey species toward collapse. Conservation measures should therefore prioritize maintaining population densities above critical thresholds and mitigating additional behavioral or environmental stressors that reduce effective reproduction or resource availability.

6.5. Nonconstant steady states exist in 1D space

To validate the theoretical predictions regarding the emergence of spatial patterns, we first consider the spatiotemporal model (2.1) in a one-dimensional spatial domain $\Omega = (0, L_x)$. The uniform discrete computational domain is defined $\Omega_d = \{x_i = (i - 0.5)\Delta x,\ 1 \le i \le N_x\}$, where $\Delta x = L_x/N_x$ is the spatial step size and N_x is the number of discrete points. Denoting the discrete approximations by $N_i^n \approx N(x_i, n\Delta t)$ and $P_i^n \approx P(x_i, n\Delta t)$, the system is integrated using an explicit Euler scheme for the time stepping. Following the finite difference approach, the system is discretized as follows [28]:

$$\begin{cases} \dfrac{N_i^{n+1} - N_i^n}{\Delta t} = d_1 \Delta_d N_i^n + N_i^n \left(\frac{\alpha N_i^n}{(\beta + N_i^n)(1 + \gamma P_i^n)} - m_1 - \delta N_i^n \right) - \frac{a N_i^n P_i^n}{1 + b N_i^n + c P_i^n} - \mu_1 (N_i^n)^2 - E_1 N_i^n, \\ \dfrac{P_i^{n+1} - P_i^n}{\Delta t} = d_2 \Delta_d P_i^n - \eta \nabla_d \cdot (P_i^n \nabla_d N_i^n) - m_2 P_i^n + \frac{\varepsilon a N_i^n P_i^n}{1 + b N_i^n + c P_i^n} - \mu_2 P_i^n - E_2 P_i^n, \end{cases}$$

where Δt is the time step size and $n = 0, 1, \ldots$. The discrete Laplacian operators are standard centered differences: $\Delta_d N_i^n = (N_{i+1}^n - 2N_i^n + N_{i-1}^n)/\Delta x^2$ and $\Delta_d P_i^n = (P_{i+1}^n - 2P_i^n + P_{i-1}^n)/\Delta x^2$. A conservative discretization is employed for the key prey-taxis term, $\nabla_d \cdot (P_i^n \nabla_d N_i^n)$:

$$\nabla_d \cdot (P_i^n \nabla_d N_i^n) = \frac{1}{\Delta x^2} \Big[P_{i+\frac{1}{2}}^n (N_{i+1}^n - N_i^n) - P_{i-\frac{1}{2}}^n (N_i^n - N_{i-1}^n) \Big],$$

with the interface values defined by linear interpolation: $P_{i+\frac{1}{2}}^n = (P_{i+1}^n + P_i^n)/2$ and $P_{i-\frac{1}{2}}^n = (P_i^n + P_{i-1}^n)/2$. Neumann boundary conditions are imposed to model a closed domain, such that $N_0^n = N_1^n$, $N_{N_x+1}^n = N_{N_x}^n$ and $P_0^n = P_1^n$, $P_{N_x+1}^n = P_{N_x}^n$.

To validate the theoretical predictions regarding the existence of Turing-driven spatial structures, we numerically solve the system (2.1) in a one-dimensional space $\Omega = (0, L_x)$. We employ a uniform discrete computational domain with $L_x = 8\pi$, utilizing $N_x = 256$ points. This yields a spatial grid size of $\Delta x = 8\pi/N_x$, and the time integration is performed with $\Delta t = 0.2\Delta x^2$ to maintain stability.

We utilize the parameter set defined in Table 2, for which the model exhibits a unique positive equilibrium point $E^* = (N^*, P^*) = (0.97, 0.32)$. The prey-taxis coefficient (η) serves as the primary bifurcation parameter.

Based on the linear stability analysis of the system, we calculated the critical taxis coefficients (η_S^k) associated with various wave numbers k:

$$\eta_S^1 \approx 1.551, \quad \eta_S^2 \approx 1.369, \quad \eta_S^3 \approx 1.147, \quad \eta_S^4 \approx 1.052, \quad \eta_S^5 \approx 0.985, \quad \ldots$$

Consequently, the minimum critical value that initiates the instability is $\eta_c = \min_{k \in \mathbb{N} \setminus \{0\}} \eta_S^k \approx 0.985$. To visually confirm the existence of stable nonconstant steady states, we select a prey-taxis coefficient below the critical threshold, namely $\eta = 0.70 < \eta_c^* = 0.985$. The simulation is initialized by perturbing the homogeneous equilibrium with a small wave corresponding to the critical wave number k_c (here $k_c = 5$ is assumed):

$$(N_0(x), P_0(x)) = \left(N^* + 0.01 \cos\left(\frac{5x}{L_x}\right), P^* + 0.01 \cos\left(\frac{5x}{L_x}\right) \right).$$

Under these conditions, the system evolves from the initial perturbation and eventually converges to a stable nonconstant steady state. This behavior confirms the theoretical prediction of the Turing instability occurring when $0 < \eta < \eta_c^*$, as illustrated in the spatial profiles shown in Figure 10 (for population $N(x,t)$) and Figure 11 (for population $P(x,t)$).

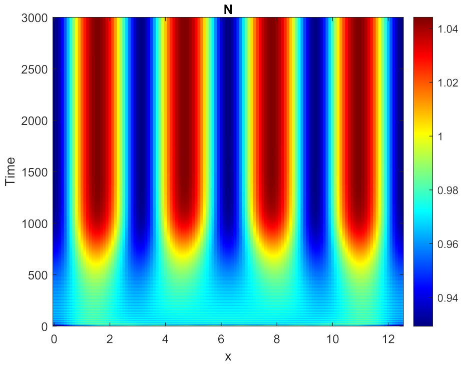

Figure 10. Nonconstant steady-state solution for the prey population $N(x)$ in 1D space.

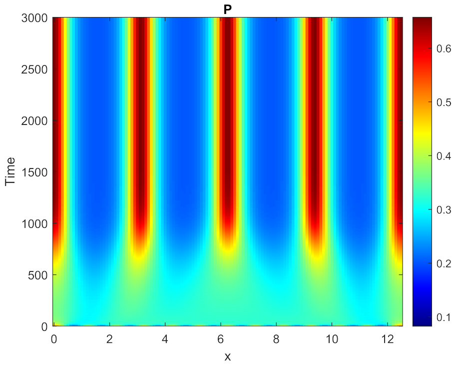

Figure 11. Nonconstant steady-state solution for the predator population $P(x)$ in 1D space.

6.6. Numerical validation of nonconstant steady states in 2D

In this subsection, we investigate the emergence of nonconstant steady states within the two-dimensional computational domain $\Omega = (0, L_x) \times (0, L_y)$. The discrete domain Ω_d is defined by a uniform mesh where $L_x = L_y = 25$ and $N_x = N_y = 128$ grid points are utilized, resulting in a spatial step size of $\Delta x = \Delta y = 25/128$. We define the discrete computational domain as

$$\Omega_d = \{(x_i, y_j)\,|\,(i-0.5)\Delta x, (j-0.5)\Delta y,\ 1 \le i \le N_x,\ 1 \le j \le N_y\},$$

where $\Delta x = L_x/N_x$ and $\Delta y = L_y/N_y$. Let $N_{ij}^n \approx N(x_i, y_j, n\Delta t)$ and $P_{ij}^n \approx P(x_i, y_j, n\Delta t)$ denote the numerical approximations. The explicit Euler method is applied to solve the system, which can be discretized as follows [28]:

$$\begin{cases} \dfrac{N_{ij}^{n+1} - N_{ij}^n}{\Delta t} = d_1 \Delta_d N_{ij}^n + N_{ij}^n \left(\dfrac{\alpha N_{ij}^n}{(\beta + N_{ij}^n)(1 + \gamma P_{ij}^n)} - m_1 - \delta N_{ij}^n \right) - \dfrac{a N_{ij}^n P_{ij}^n}{1 + b N_{ij}^n + c P_{ij}^n} \\ \qquad\qquad - \mu_1 (N_{ij}^n)^2 - E_1 N_{ij}^n, \\ \dfrac{P_{ij}^{n+1} - P_{ij}^n}{\Delta t} = d_2 \Delta_d P_{ij}^n - \eta \nabla_d \cdot (P_{ij}^n \nabla_d N_{ij}^n) - m_2 P_{ij}^n + \dfrac{\varepsilon a N_{ij}^n P_{ij}^n}{1 + b N_{ij}^n + c P_{ij}^n} - \mu_2 P_{ij}^n - E_2 P_{ij}^n, \end{cases}$$

where the two-dimensional discrete Laplacian operators are defined by

$$\Delta_d N^n_{ij} = \frac{N^n_{i+1,j} - 2N^n_{ij} + N^n_{i-1,j}}{\Delta x^2} + \frac{N^n_{i,j+1} - 2N^n_{ij} + N^n_{i,j-1}}{\Delta y^2},$$

$$\Delta_d P^n_{ij} = \frac{P^n_{i+1,j} - 2P^n_{ij} + P^n_{i-1,j}}{\Delta x^2} + \frac{P^n_{i,j+1} - 2P^n_{ij} + P^n_{i,j-1}}{\Delta y^2}.$$

A conservative discretization is adopted for the taxis term:

$$\begin{aligned}\nabla_d\cdot(P^n_{ij}\nabla_d N^n_{ij}) = {} & \frac{1}{\Delta x^2}\Big[P^n_{i+\frac{1}{2},j}(N^n_{i+1,j} - N^n_{ij}) - P^n_{i-\frac{1}{2},j}(N^n_{ij} - N^n_{i-1,j})\Big] \\ & + \frac{1}{\Delta y^2}\Big[P^n_{i,j+\frac{1}{2}}(N^n_{i,j+1} - N^n_{ij}) - P^n_{i,j-\frac{1}{2}}(N^n_{ij} - N^n_{i,j-1})\Big],\end{aligned}$$

where the midpoint values are computed as

$$P^n_{i+\frac{1}{2},j} = \tfrac{1}{2}\Big(P^n_{i+1,j} + P^n_{ij}\Big), \qquad P^n_{i-\frac{1}{2},j} = \tfrac{1}{2}\Big(P^n_{i-1,j} + P^n_{ij}\Big),$$

$$P^n_{i,j+\frac{1}{2}} = \tfrac{1}{2}\Big(P^n_{i,j+1} + P^n_{ij}\Big), \qquad P^n_{i,j-\frac{1}{2}} = \tfrac{1}{2}\Big(P^n_{i,j-1} + P^n_{ij}\Big).$$

The resulting explicit numerical scheme is

$$\begin{cases} N^{n+1}_{ij} = N^n_{ij} + \Delta t\Big[d_1\Delta_d N^n_{ij} + N^n_{ij}\Big(\frac{\alpha N^n_{ij}}{(\beta+N^n_{ij})(1+\gamma P^n_{ij})} - m_1 - \delta N^n_{ij}\Big) - \frac{aN^n_{ij}P^n_{ij}}{1+bN^n_{ij}+cP^n_{ij}} \\ \qquad\qquad - \mu_1(N^n_{ij})^2 - E_1N^n_{ij}\Big], \\ P^{n+1}_{ij} = P^n_{ij} + \Delta t\Big[d_2\Delta_d P^n_{ij} - \eta\,\nabla_d\cdot(P^n_{ij}\nabla_d N^n_{ij}) - m_2P^n_{ij} + \frac{\varepsilon aN^n_{ij}P^n_{ij}}{1+bN^n_{ij}+cP^n_{ij}} - \mu_2P^n_{ij} - E_2P^n_{ij}\Big]. \end{cases}$$

The resulting numerical scheme is first-order accurate in time due to the explicit Euler discretization and second-order accurate in space owing to the central finite-difference approximation of the Laplacian and gradient operators. Neumann boundary conditions are imposed as $N^n_{0,j} = N^n_{1,j}$, $N^n_{N_x+1,j} = N^n_{N_x,j}$, $N^n_{i,0} = N^n_{i,1}$, $N^n_{i,N_y+1} = N^n_{i,N_y}$, and similarly for P.

For the two-dimensional numerical analysis, the steady state is considered attained (N^s, P^s) when the average discrete l^2-error between successive time steps drops below a specified tolerance tol. This is defined as $0.5(\text{Error}^s_N + \text{Error}^s_P) < \text{tol}$. In our numerical experiments, we established the tolerance at $\text{tol} = 1.0 \times 10^{-6}$. We utilize a uniform mesh with $N_x = N_y = 128$ points, a spatial domain $\Omega = (0, 25) \times (0, 25)$, and a time step $\Delta t = 0.2\Delta x^2$. To ensure numerical stability of the explicit Euler scheme, the time step is chosen according to a Courant-Friedrichs-Lewy (CFL) type condition associated with the diffusive terms. In two space dimensions, stability of the explicit discretization of the Laplacian requires

$$\Delta t \le \frac{1}{4}\min\left(\frac{\Delta x^2}{d_1}, \frac{\Delta x^2}{d_2}\right).$$

The choice $\Delta t = 0.2\,\Delta x^2$ satisfies this stability constraint for the parameter values considered. The simulation is initialized using a randomly perturbed initial condition around the unique positive equilibrium $E^* = (N^*, P^*) = (0.97, 0.32)$:

$$N(x, y, 0) = N^* + 0.01 \cdot \text{rand}(x, y), \quad P(x, y, 0) = P^* + 0.01 \cdot \text{rand}(x, y),$$

where rand(x,y) is a random variable between −1 and 1. For the set of parameters provided in Table 2, the critical prey-taxis sensitivity constant for the onset of the steady-state bifurcation is determined as $\eta_c \approx 0.985$. To verify that the observed spatial patterns are not numerical artifacts, additional simulations were performed using refined spatial meshes (e.g., 256×256). The qualitative structure of the patterns remained unchanged, confirming the robustness of the numerical results with respect to spatial discretization.

Scenario 1: Isolated spot patterns ($\eta = 0.75$)**.**

We first consider the prey–taxis coefficient $\eta = 0.75$, which satisfies $\eta < \eta_c^* = 0.985$ and therefore lies within the Turing instability regime. Starting from a small random perturbation around the homogeneous equilibrium, the system evolves toward a pattern dominated by isolated spots distributed over the spatial domain. The resulting stable nonconstant steady states are illustrated in Figures 12 and 13, where both prey and predator densities exhibit localized spot-like structures.

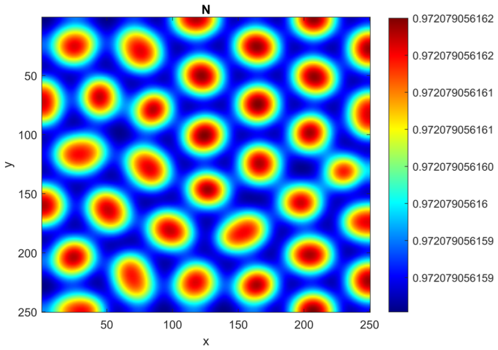

Figure 12. Nonconstant stationary pattern (prey, N) obtained with the prey–taxis coefficient $\eta = 0.75 < \eta_c^* = 0.985$. Since the taxis intensity lies within the Turing instability regime, the homogeneous equilibrium loses stability and the system evolves toward an isolated spot pattern distributed over the spatial domain.

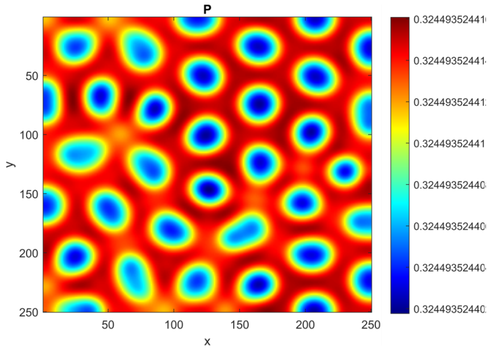

Figure 13. Nonconstant stationary pattern (predator, P) obtained with the prey–taxis coefficient $\eta = 0.75 < \eta_c^* = 0.985$. The predator population forms localized spot aggregates corresponding to the prey spatial distribution, confirming the emergence of taxi-induced Turing patterns.

Scenario 2: Mixed spot–stripe patterns ($\eta = 0.90$)**.**

Next, we increase the prey–taxis coefficient to $\eta = 0.90$, which still satisfies $\eta < \eta_c^*$ and remains in the Turing instability regime. Under this higher taxis intensity, the spatial structures become more connected and evolve toward a mixed pattern consisting of labyrinth-like stripes together with spot aggregates. The corresponding stationary spatial distributions are presented in Figures 14 and 15.

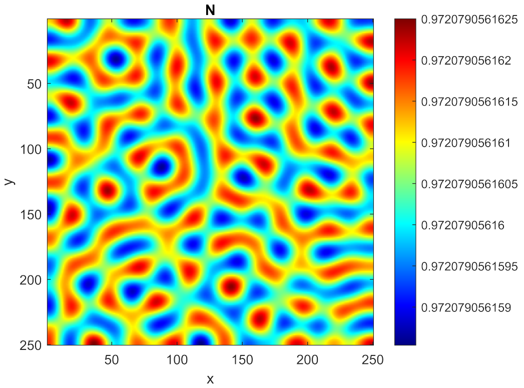

Figure 14. Nonconstant stationary pattern (prey, N) obtained with the prey–taxis coefficient $\eta = 0.90 < \eta_c^* = 0.985$. Since the taxis intensity still lies within the Turing instability regime, the system develops a mixed spot–stripe pattern composed of labyrinth-like stripes and localized spots.

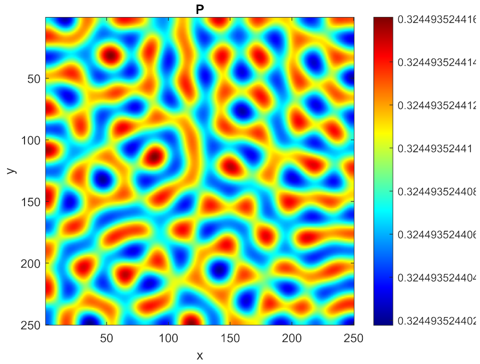

Figure 15. Nonconstant stationary pattern (predator, P) obtained with the prey–taxis coefficient $\eta = 0.90 < \eta_c^* = 0.985$. The predator distribution exhibits a stable mixed spatial structure consisting of stripes and spot aggregates, reflecting the taxi-induced spatial organization of the populations.

6.7. Numerical analysis of pattern formation on spherical and cubic surfaces

In this subsection, we extend our numerical investigation of the nonconstant steady states of system (1) to two complex geometries: a smooth closed spherical surface (S_h) and a three-dimensional cubic volume (Ω). We employ the explicit Euler scheme for time integration across both models, while using geometry-appropriate methods for spatial discretization. Time integration was performed using an explicit Euler scheme with

$$\Delta t = 0.2\ \min(\Delta x^2, \Delta y^2, \Delta z^2),$$

chosen to satisfy a CFL-type stability condition associated with the diffusion operators and to ensure numerical stability. Additional tests with smaller time steps confirmed that the qualitative features of the emerging spatial patterns remained unchanged.

6.7.1. Discretization on a spherical surface

To investigate pattern formation on a smooth closed surface S_h, such as a spherical surface, we utilize a triangulated mesh where $\{x_i\}_{i=1}^n$ denotes the discrete set of surface points. The mesh was generated following standard procedures based on the cotangent Laplace–Beltrami approximation [28], providing uniform coverage of the curved domain. The corresponding code for generating the mesh and implementing the numerical scheme is provided in the Supplementary Material. The numerical approximations N_i^n and P_i^n are obtained using the following discrete scheme [28]:

$$\begin{cases} \dfrac{N_i^{n+1} - N_i^n}{\Delta t} = d_1 \Delta_S N_i^n + N_i^n \left(\frac{\alpha N_i^n}{(\beta + N_i^n)(1+\gamma P_i^n)} - m_1 - \delta N_i^n \right) - \frac{a N_i^n P_i^n}{1 + b N_i^n + c P_i^n} - \mu_1 (N_i^n)^2 - E_1 N_i^n, \\ \dfrac{P_i^{n+1} - P_i^n}{\Delta t} = d_2 \Delta_S P_i^n - \eta \nabla_S \cdot (P_i^n \nabla_S N_i^n) - m_2 P_i^n + \frac{\varepsilon a N_i^n P_i^n}{1 + b N_i^n + c P_i^n} - \mu_2 P_i^n - E_2 P_i^n, \end{cases}$$

where the discrete Laplace–Beltrami operator Δ_S is defined using the cotangent formula:

$$\Delta_S N_i = \frac{3}{\mathcal{A}(x_i)} \sum_{j \in I(i)} \frac{\cot \alpha_{ij} + \cot \beta_{ij}}{2} (N_j - N_i), \qquad \Delta_S P_i = \frac{3}{\mathcal{A}(x_i)} \sum_{j \in I(i)} \frac{\cot \alpha_{ij} + \cot \beta_{ij}}{2} (P_j - P_i),$$

with $\mathcal{A}(x_i)$ representing the cumulative area of the one-ring triangles associated with vertex x_i. The discrete divergence term on the spherical surface is approximated in its conservative form as

$$\nabla_S \cdot (P_i^n \nabla_S N_i^n) = \frac{3\eta}{\mathcal{A}(x_i)} \sum_{j \in I(i)} \frac{\cot \alpha_{ij} + \cot \beta_{ij}}{2} \left(\frac{P_j^n + P_i^n}{2} \right) (N_j^n - N_i^n).$$

The simulation is initialized with a randomly perturbed condition around the equilibrium (N^*, P^*):

$$\begin{cases} N(x_i, 0) = N^* + 0.02 \, \mathrm{rand}(x_i), \\ P(x_i, 0) = P^* + 0.02 \, \mathrm{rand}(x_i), \end{cases}$$

where $\mathrm{rand}(x_i)$ is a uniformly distributed random number in $[-1, 1]$.

For the spherical domain (radius $r = 15$), we select a prey–taxis coefficient $\eta = 0.90$, which satisfies $\eta < \eta_c^* = 0.985$ and therefore lies within the Turing instability regime identified in the planar analysis. Under this condition, the system evolves toward a spotted spatial pattern distributed across the spherical surface. The corresponding stable nonconstant steady states for the prey (N) and predator (P) populations are presented in Figures 16 and 17, respectively.

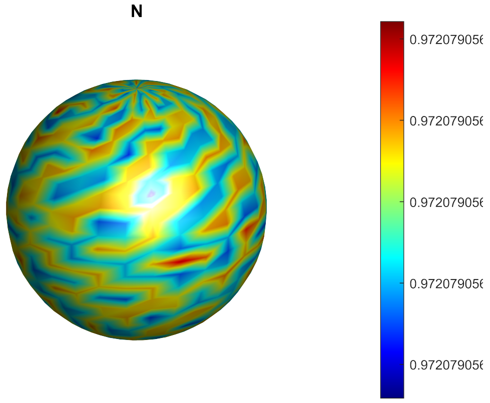

Figure 16. Nonconstant stationary pattern of prey (N) on a spherical surface (radius $r = 15$), obtained with the prey–taxis coefficient $\eta = 0.90 < \eta_c^* = 0.985$.

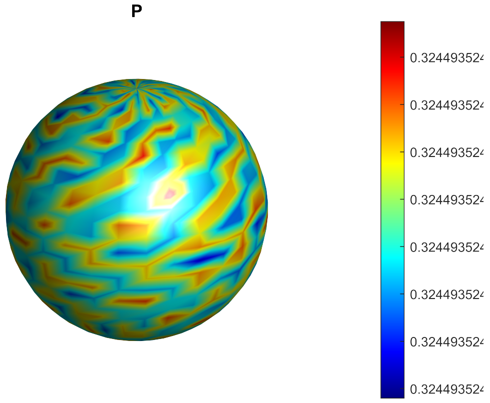

Figure 17. Nonconstant stationary pattern of predators (P) on a spherical surface (radius $r = 15$), obtained with the prey–taxis coefficient $\eta = 0.90 < \eta_c^* = 0.985$.

The persistence of spatial heterogeneity across planar, spherical, and cubic geometries indicates that prey–taxis generates structurally robust aggregation patterns that are not artifacts of the domain shape. Ecologically, such spotted or patchy distributions may represent predator aggregation hotspots or localized prey refuges in marine environments. These emergent structures suggest that predator pressure becomes spatially concentrated rather than uniformly distributed, potentially increasing extinction risk within high density patches while leaving other regions underexploited. From a management perspective, this observation highlights the importance of accounting for spatial aggregation processes when designing marine protected areas or regulating harvesting effort, since local overexploitation may occur even when the global biomass appears stable.

6.7.2. Discretization in a cubic surface

We also investigate the spatiotemporal dynamics of system (1) in the three-dimensional cubic domain $\Omega = (0, L_x) \times (0, L_y) \times (0, L_z)$ [29]. The domain is uniformly discretized, and the numerical approximations $N^n_{i,j,k}$ and $P^n_{i,j,k}$ are obtained via the explicit Euler scheme:

$$\begin{cases} \dfrac{N^{n+1}_{i,j,k} - N^n_{i,j,k}}{\Delta t} = d_1 \Delta_d N^n_{i,j,k} + N^n_{i,j,k}\left(\frac{\alpha N^n_{i,j,k}}{(\beta + N^n_{i,j,k})(1+\gamma P^n_{i,j,k})} - m_1 - \delta N^n_{i,j,k}\right) - \frac{a N^n_{i,j,k} P^n_{i,j,k}}{1 + b N^n_{i,j,k} + c P^n_{i,j,k,}} \\ \qquad\qquad - \mu_1 (N^n_{i,j,k})^2 - E_1 N^n_{i,j,k}, \\ \dfrac{P^{n+1}_{i,j,k} - P^n_{i,j,k}}{\Delta t} = d_2 \Delta_d P^n_{i,j,k} - \eta \nabla_d \cdot (P^n_{i,j,k} \nabla_d N^n_{i,j,k}) - m_2 P^n_{i,j,k} + \frac{\varepsilon a N^n_{i,j,k} P^n_{i,j,k}}{1 + b N^n_{i,j,k} + c P^n_{i,j,k}} - \mu_2 P^n_{i,j,k,} \\ \qquad\qquad - E_2 P^n_{i,j,k}, \end{cases}$$

where the three-dimensional discrete Laplacian operator is defined by standard centered differences:

$$\Delta_d N^n_{i,j,k} = \frac{N^n_{i+1,j,k} - 2N^n_{i,j,k} + N^n_{i-1,j,k}}{\Delta x^2} + \frac{N^n_{i,j+1,k} - 2N^n_{i,j,k} + N^n_{i,j-1,k}}{\Delta y^2} + \frac{N^n_{i,j,k+1} - 2N^n_{i,j,k} + N^n_{i,j,k-1}}{\Delta z^2},$$

and similarly for $\Delta_d P^n_{i,j,k}$. The conservative discretization of the taxis term is extended to 3D as

$$\begin{aligned} \nabla_d \cdot (P^n_{i,j,k} \nabla_d N^n_{i,j,k}) = {} & \frac{1}{\Delta x^2}\Big[P^n_{i+\frac{1}{2},j,k}(N^n_{i+1,j,k} - N^n_{i,j,k}) - P^n_{i-\frac{1}{2},j,k}(N^n_{i,j,k} - N^n_{i-1,j,k})\Big] \\ & + \frac{1}{\Delta y^2}\Big[P^n_{i,j+\frac{1}{2},k}(N^n_{i,j+1,k} - N^n_{i,j,k}) - P^n_{i,j-\frac{1}{2},k}(N^n_{i,j,k} - N^n_{i,j-1,k})\Big] \\ & + \frac{1}{\Delta z^2}\Big[P^n_{i,j,k+\frac{1}{2}}(N^n_{i,j,k+1} - N^n_{i,j,k}) - P^n_{i,j,k-\frac{1}{2}}(N^n_{i,j,k} - N^n_{i,j,k-1})\Big], \end{aligned}$$

where half-index values are computed using linear averaging. Homogeneous Neumann boundary conditions are applied on all faces of the cubic domain.

Choosing a prey–taxis coefficient within the Turing instability regime, for instance $\eta = 0.9 < \eta^*_c = 0.985$, the three–dimensional simulation reveals complex internal structures, such as tubular or sheet–like patterns, which differ from the simpler spot patterns observed in two dimensional domains. Cross sections illustrating the stable three-dimensional spatial distributions of the prey (N) and predator (P) populations are displayed in Figures 18 and 19.

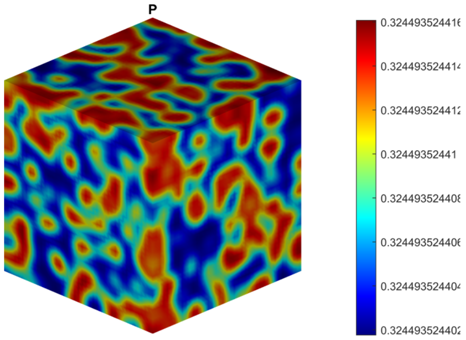

Figure 18. Cross-section of the nonconstant stationary pattern for prey (N) in the 3D cubic domain, obtained with the prey–taxis coefficient $\eta = 0.9 < \eta_c^* = 0.985$.

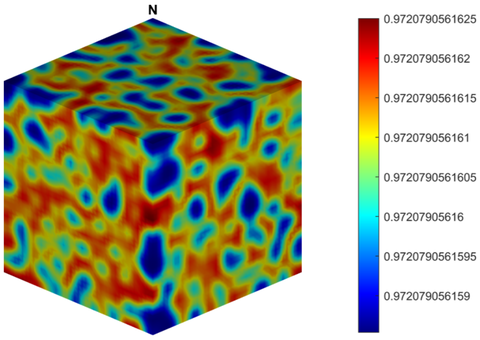

Figure 19. Cross-section of the nonconstant stationary pattern for predators (P) in the 3D cubic domain, obtained with the prey–taxis coefficient $\eta = 0.9 < \eta_c^* = 0.985$.

The numerical simulations presented in this study validate the theoretical predictions regarding spatial pattern emergence and global stability constraints, enabling a meaningful comparison with contemporary research in spatiotemporal ecological systems. Our central numerical finding is that prey–taxis (η) acts as a key mechanism driving Turing instability in this highly nonlinear system. In particular, the calculated critical threshold $\eta_c^* \approx 0.985$ accurately predicts the onset of spatial pattern formation. This result is consistent with the findings of [28], who reported that directed movement mechanisms can act as destabilizing forces capable of generating spatial heterogeneity in ecological systems, especially when additional external pressures such as harvesting are present.

Our simulations further indicate that increasing the taxis coefficient toward the critical threshold (e.g., $\eta = 0.90$) leads to more localized spot–like aggregates. This behavior highlights the dual role of prey–taxis: Moderate taxis intensities promote spatial self–organization, whereas values exceeding the critical threshold η_c^* eventually restore the stability of the homogeneous equilibrium and suppress spatial patterns. Similar mechanisms have been observed in several reaction–advection–diffusion models [30–32], where directed movement both triggers spatial instability and regulates pattern morphology.

The weakly nonlinear (WNL) analysis and the resulting pattern selection observed in our simulations reveal a transition from isolated spot patterns ($\eta = 0.75$) to more complex mixed stripe–spot structures ($\eta = 0.90$). This pattern complexity extends beyond the simple stripe structures typically associated with classical Turing systems. The use of weakly nonlinear analysis to characterize amplitude bifurcations aligns closely with the methodological approach and findings reported by [33], who investigated pattern formation in systems incorporating hunting cooperation and chemotaxis.

As in their study, our results demonstrate that the interaction between nonlinear ecological mechanisms (such as the Beddington–DeAngelis functional response, fear effects, and the Allee effect) and directed movement plays a crucial role in generating higher–order spatial patterns, including hexagonal and mixed structures. These results indicate that the resulting ecological patterns are not solely determined by diffusion coefficients but instead emerge from the complex nonlinear interactions governing the system dynamics near the homogeneous equilibrium.

Furthermore, the successful emergence of spatial patterns on different geometries, including planar, spherical, and cubic domains, indicates that spatial self–organization is an intrinsic property of the model dynamics rather than an artifact of a particular domain shape. Comparable observations were reported by [34] and more recently by [35], who demonstrated that spatial curvature and domain topology can influence pattern persistence and wavelength selection in ecological reaction–diffusion systems.

Beyond the spatial domain, our analysis of the two-parameter bifurcation diagrams provides a critical hierarchy of threats to ecosystem persistence. The most significant result in this domain is establishing the Allee threshold (β) as the ultimate determinant of the system's fate, controlling the boundaries of Hopf oscillation and saddle-node extinction. This finding contrasts sharply with models that focus primarily on interspecific interactions as the main drivers of instability. For instance, while [36] demonstrated that hunting cooperation plays a crucial role in shifting the Turing threshold and influencing stability in a Holling type III model, our results suggest that the demographic bottleneck imposed by the Allee effect (β) constitutes a more fundamental and less malleable constraint on long-term survival than behavioral or purely trophic dynamics alone. Similar insights were obtained by [37] and [38], who emphasized the role of critical thresholds in determining extinction or persistence regimes in ecological systems. Biologically, this distinction is vital for conservation, suggesting that strategies must prioritize preventing population density from falling below the critical Allee threshold over mitigating the effects of fear or competition. Complementing this, the fear intensity (γ) and conversion efficiency (ε) were confirmed to act as secondary density modulators: The contour plots illustrate that increasing γ or ε leads to a monotonic reduction in the prey's carrying capacity, a finding consistent with studies in behavioral ecology that link fear to reduced foraging and reproductive effort [39,40], thereby suppressing population levels without triggering immediate extinction. Conclusively, this synthesis of results validates the crucial role of taxis in pattern formation while simultaneously providing a clear, parameter-driven ranking of threats essential for effective ecological management.

6.8. Limitations and perspectives

While the numerical simulations robustly validate the theoretical predictions and illustrate the emergence of diverse spatial patterns across planar, spherical, and cubic domains, several limitations should be acknowledged.

First, the model assumes a homogeneous environmental toxicity and uniform habitat conditions. In natural ecosystems, spatial heterogeneity in resource availability, pollution, or habitat structure can significantly affect predator-prey interactions and pattern formation, potentially altering both the type and stability of emergent structures.

Second, the predator functional response is modeled without accounting for handling time or satiation effects. This simplification may overestimate predation pressure at high prey densities and affect the predicted thresholds for Turing instability or pattern selection.

Third, the simulations are performed over finite, relatively short time scales. Long-term dynamics, transient phenomena, or stochastic environmental fluctuations may lead to qualitative changes in population distributions that are not captured in the current deterministic framework.

Finally, while the extension to spherical and cubic geometries provides insights into topological effects on pattern formation, the ecological implications of these complex spatial structures require further investigation. In particular, the consequences for predator aggregation, prey refuges, and local extinction risk in real marine or terrestrial habitats are not fully addressed.

Future work should incorporate heterogeneous environmental conditions, more realistic functional responses, stochastic perturbations, and longer simulation periods. Such extensions would enhance the ecological realism of the model and provide more robust guidance for conservation management and spatial planning in ecosystems exhibiting prey-taxis and other spatially dependent interactions.

7. Conclusions

In this work, we proposed and thoroughly investigated the spatiotemporal dynamics of the predator-prey system, which comprehensively integrates critical ecological factors rarely combined in a single framework: the Allee effect β, the fear effect γ, the Beddington–DeAngelis functional response, and the stabilizing effect of predator prey-taxis η within a harvested and toxic environment. Our theoretical foundation confirmed the system's well-posedness by establishing the existence and boundedness of classical solutions. Focusing on the homogeneous steady state, linear stability analysis identified Turing instability as the crucial mechanism for generating spatial heterogeneity. This instability, which gives rise to nonhomogeneous pattern formation, was shown to be the joint effect of the predator's directed movement prey-taxis η and the differential diffusion rates d_1, d_2. We established that prey-taxis is essential for inducing pattern formation, but similar to the destabilizing effects seen in other cross-diffusion systems, a sufficiently large taxis coefficient η can annihilate spatial patterns and return the system to a coexisting homogeneous steady state. Furthermore, by employing weakly nonlinear analysis (WNL) and deriving the relevant amplitude equations, we predicted the existence and stability of various heterogeneous patterns, including hexagonal spots, stripes, and mixed structures. These theoretical predictions were rigorously validated through extensive numerical simulations, which demonstrated the emergence of complex patterns across two, and three-dimensional domains. Crucially, our analysis of the two-parameter bifurcation diagrams revealed that the Allee threshold β is the ultimate determinant of the system's survival, controlling both the onset of oscillations (Hopf bifurcation) and the final boundary of irreversible extinction (saddle-node bifurcation), while the fear intensity γ and conversion efficiency ε primarily function as density modulators. Overall, this study underscores the significant role of complex behavioral and demographic factors in driving spatiotemporal structuring, offering critical insights for the effective management and conservation of vulnerable marine ecosystems. Overall, our results demonstrate a clear hierarchy of ecological drivers: The Allee threshold (β) governs species persistence and extinction boundaries, while prey-taxis (η) governs spatial self-organization and aggregation. Fear intensity (γ) and conversion efficiency (ε) modulate population densities within the viable domain but do not determine persistence thresholds. This separation of roles has important implications for marine ecosystem management: Maintaining population densities above critical Allee thresholds is essential for preventing collapse, while spatial aggregation mechanisms must be considered to avoid localized depletion caused by predator clustering. Ignoring taxis-driven spatial heterogeneity may therefore lead to an underestimation of extinction risks in spatially structured marine systems.

Use of AI tools declaration

The authors declare they have not used Artificial Intelligence (AI) tools in the creation of this article.

Conflict of interest

The authors declare there is no conflict of interest.

References

1. C. Li, Protecting endangered animal species, *Animals*, **14** (2024), 2644. https://doi.org/10.3390/ani14182644
2. A. J. Lotka, *Elements of Physical Biology*, Williams & Wilkins, Baltimore, 1925.
3. A. J. Lotka, Fluctuations in the abundance of a species considered mathematically, *Nature*, **119** (1927), 12. https://doi.org/10.1038/119012a0
4. A. M. Turing, The chemical basis of morphogenesis, *Philos Trans. R. Soc. Lond. B Biol. Sci.*, **237** (1952), 37–72. https://doi.org/10.1098/rstb.1952.0012
5. M. Hafdane, N. Baba, Y. E. Foutayeni, N. Achtaich, Dynamic complexity of a delayed spatiotemporal predator-prey model, *Front. Appl. Math. Stat.*, **11** (2025), 1523276. https://doi.org/10.3389/fams.2025.1523276
6. K. Al Amri, Q. J. A. Khan, D. Greenhalgh, Combined impact of fear and Allee effect in predator-prey interaction models, *Math. Biosci. Eng.*, **21** (2024), 7211–7252. https://doi.org/10.3934/mbe.2024319
7. D. Pal, D. Kesh, D. Mukherjee, Dynamics of a predator–prey model with fear and its carryover effects, *Int. J. Bifurcation Chaos*, **35** (2025), 2550073. https://doi.org/10.1142/S0218127425500737
8. D. Grünbaum, Using spatially explicit models to characterize foraging performance in heterogeneous landscapes, *Am. Nat.*, **151** (1998), 97–113.
9. W. W. Murdoch, J. Chesson, P. L. Chesson, Biological control in theory and practice, *Am. Nat.*, **125** (1985), 344–366.
10. N. Sapoukhina, Y. Tyutyunov, R. Arditi, The role of prey taxis in biological control: A spatial theoretical model, *Am. Nat.*, **162** (2003), 61–76.
11. P. Kareiva, G. Odell, Swarms of predators exhibit preytaxis if individual predators use area-restricted search, *Am. Nat.*, **130** (1987), 233–270.
12. H. Y. Jin, Z. A. Wang, Global stability of prey-taxis systems, *J. Differ. Equations*, **262** (2017), 1257–1290. https://doi.org/10.1016/j.jde.2016.10.010
13. R. Han, S. Dey, J. Huang, M. Banerjee, Spatio-temporal steady-state analysis in a prey–predator model with saturated hunting cooperation and chemotaxis, *Acta Appl. Math.*, **191** (2024), 10. https://doi.org/10.1007/s10440-024-00658-x
14. S. Wu, J. Shi, B. Wu, Global existence of solutions and uniform persistence of a diffusive predator–prey model with prey-taxis, *J. Differ. Equations*, **260** (2016), 5847–5874. https://doi.org/10.1016/j.jde.2015.12.024

15. W. Tao, Z. A. Wang, Global well-posedness and Turing-Hopf bifurcation of prey-taxis systems with hunting cooperation, *Eur. J. Appl. Math.* (2025), 1–27. https://doi.org/10.1017/S0956792525000026

16. S. Kondo, R. Asai, A reaction–diffusion wave on the skin of the marine angelfish Pomacanthus, *Nature*, **376** (1995), 765–768. https://doi.org/10.1038/376765a0

17. R. A. Cangelosi, D. J. Wollkind, B. J. Kealy-Dichone, I. Chaiya, Nonlinear stability analyses of Turing patterns for a mussel-algae model, *J. Math. Biol.*, **70** (2015), 1249–1294. https://doi.org/10.1007/s00285-014-0794-7

18. A. M. Turing, The chemical basis of morphogenesis, *Bull. Math. Biol.*, **52** (1990), 153–197. https://doi.org/10.1007/BF02459572

19. S. Petrovskii, H. Malchow, Wave of chaos: New mechanism of pattern formation, *Theor. Popul. Biol.*, **59** (2001), 157–174. https://doi.org/10.1006/tpbi.2000.1507

20. J. A. Sherratt, Periodic travelling waves in cyclic predator-prey systems, *Ecol. Lett.*, **4** (2001), 30–37. https://doi.org/10.1046/j.1461-0248.2001.00197.x

21. W. Wang, X. Q. Zhao, Basic reproduction numbers for reaction–diffusion epidemic models, *SIAM J. Appl. Dyn. Syst.*, **11** (2012), 1652–1673. https://doi.org/10.1137/120872942

22. J. D. Murray, *Mathematical Biology: II: Spatial Models and Biomedical Applications*, 3rd edition, Springer, New York, 2003.

23. P. Arena, S. Baglio, L. Fortuna, G. Manganaro, Self-organization in a two-layer CNN, *IEEE Trans. Circuits Syst. I: Fund. Theory Appl.*, **45** (2002), 157–162. https://doi.org/10.1109/81.993231

24. F. J. Ni, G. B. Arhonditsis, Examination of the effects of toxicity and nutrition on a two-prey one-predator system with a metabolomics-inspired model, *Ecol. Inf.*, **73** (2023), 101905. https://doi.org/10.1016/j.ecoinf.2022.101905

25. H. Amann, Dynamic theory of quasilinear parabolic equations. II. Reaction-diffusion systems, *Differ. Integr. Equations*, **3** (1990), 13–75.

26. S. Wu, J. Shi, B. Wu, Global existence of solutions and uniform persistence of a diffusive predator–prey model with prey-taxis, *J. Differ. Equations*, **260** (2016), 5847–5874. https://doi.org/10.1016/j.jde.2015.12.024

27. R. Garver, On the nature of the roots of a quartic equation, *Math. News Lett.*, **7** (1933), 6–8. https://doi.org/10.2307/3027447

28. M. Chen, C. Tian, S. Ham, H. Kim, J. Kim, Impact of prey-taxis on a harvested intraguild predation predator–prey model, *Eur. J. Appl. Math.* (2025), 1–38. https://doi.org/10.1017/S0956792525000087

29. Z. Bi, S. Liu, M. Ouyang, Three-dimensional pattern dynamics of a fractional predator–prey model with cross-diffusion and herd behavior, *Appl. Math. Comput.*, **421** (2022), 126955. https://doi.org/10.1016/j.amc.2022.126955

30. M. Banerjee, S. Petrovskii, Self-organised spatial patterns and chaos in a ratio-dependent predator-prey system, *Theor. Ecol.*, **4** (2011), 37–53. https://doi.org/10.1007/s12080-010-0073-1

31. Z. Wang, L. Zhao, S. Ruan, Turing patterns in reaction–advection–diffusion systems, *Chaos Solitons Fractals*, **125** (2019), 161–172. https://doi.org/10.1016/j.chaos.2019.04.023

32. D. Xiao, S. Ruan, Spatiotemporal dynamics in predator–prey systems with diffusion and taxis, *Nonlinear Anal. Real World Appl.*, **58** (2021), 103202. https://doi.org/10.1016/j.nonrwa.2020.103202

33. H. Rahmani, D. Saadi, E. Dads, S. Benamara, Weakly nonlinear analysis and pattern formation in a predator-prey system with cross-diffusion and hunting cooperation, *Acta Appl. Math.*, **188** (2023), 1–36.

34. A. B. Medvinsky, D. Tikhonov, H. Malchow, S. Petrovskii, Spatiotemporal complexity of plankton and fish dynamics, *Rev. Mod. Phys.*, **74** (2002), 591–641. https://doi.org/10.1103/RevModPhys.74.591

35. K. Kuto, Y. Nagahara, T. Takahashi, Pattern formation on curved surfaces in reaction-diffusion systems, *J. Math. Biol.*, **80** (2020), 193–223. https://doi.org/10.1007/s00285-019-01434-5

36. S. Benamara, H. Rahmani, E. Dads, K. Djebbar, Qualitative analysis for a diffusive predator–prey model with hunting cooperation and Holling type III functional response, *Nonlinear Anal. Real World Appl.*, **73** (2023), 10392.

37. F. Berezovskaya, G. Karev, R. Arditi, Allee effects and resilience in ecological models, *Math. Biosci.*, **197** (2005), 173–187. https://doi.org/10.1016/j.mbs.2005.04.003

38. M. Rietkerk, J. van de Koppel, Regular pattern formation in real ecosystems, *Trends Ecol. Evol.*, **23** (2008), 169–175. https://doi.org/10.1016/j.tree.2007.10.013

39. Y. Zhan, W. Li, J. Zhang, Fear effects and behavioral responses in predator–prey interactions: A modeling approach, *Ecol. Model.*, **483** (2023), 110409. https://doi.org/10.1016/j.ecolmodel.2023.110409

40. P. Abrams, Fear, foraging, and population regulation: Revisiting non-consumptive effects in predator-prey systems, *Ecol. Lett.*, **25** (2022), 317–331. https://doi.org/10.1111/ele.13912

Appendix

A. Technical estimates for Lemma 5

A.1. Control of mixed gradient terms

(i) Estimate of the cross term involving $\Psi'(N)\nabla N \cdot \nabla P$. Using Young's inequality, we find

$$\begin{aligned}-(d_1+d_2)\int_\Omega P^{m-1}\Psi'(N)\,\nabla N\cdot\nabla P\,dx \le{}& \frac{d_2(m-1)}{4}\int_\Omega P^{m-2}\Psi(N)\,|\nabla P|^2\,dx\\ &+4\rho^4\frac{(d_1+d_2)^2}{d_2(m-1)}\int_\Omega P^m N^2\Psi(N)\,|\nabla N|^2\,dx.\end{aligned}$$

(ii) Estimate of the cross term with $\eta(m-1)\Psi(N)\nabla N\cdot\nabla P$. Again by Young's inequality,

$$\begin{aligned}\eta(m-1)\int_\Omega P^{m-1}\Psi(N)\,\nabla N\cdot\nabla P\,dx \le{}& \frac{d_2(m-1)}{4}\int_\Omega P^{m-2}\Psi(N)\,|\nabla P|^2\,dx\\ &+\frac{\eta^2(m-1)}{d_2}\int_\Omega P^m\Psi(N)\,|\nabla N|^2\,dx.\end{aligned}$$

Collecting all the above estimates, we finally arrive at

$$\begin{aligned}\frac{1}{m}\frac{d}{dt}\int_\Omega P^m\Psi(N)\,dx &+\frac{d_2(m-1)}{2}\int_\Omega P^{m-2}\Psi(N)\,|\nabla P|^2\,dx+\frac{d_1}{m}\int_\Omega P^m\Psi''(N)\,|\nabla N|^2\,dx\\ &\le 4\rho^4\frac{(d_1+d_2)^2}{d_2(m-1)}\int_\Omega P^mN^2\Psi(N)\,|\nabla N|^2\,dx\\ &\quad+\frac{\eta^2(m-1)}{d_2}\int_\Omega P^m\Psi(N)\,|\nabla N|^2\,dx+\eta\int_\Omega P^m\Psi'(N)\,|\nabla N|^2\,dx\\ &\quad+\left(\frac{\varepsilon a}{b}+\frac{2\rho^2\alpha C_1^2}{m}\right)\int_\Omega P^m\Psi(N)\,dx.\end{aligned}$$

We define the following functions:

$$f_1(s)=4\rho^4\,\frac{(d_1+d_2)^2}{d_2(m-1)}\,s^2\Psi(s),\qquad f_2(s)=\frac{\eta^2(m-1)}{d_2}\,\Psi(s),$$

$$f_3(s)=2\rho^2\eta\,s\,\Psi(s),\qquad f_4(s)=\frac{2\rho^2d_1}{m}\,\Psi(s)+\frac{4\rho^4d_1}{m}\,s^2\Psi(s).$$

Then, the following estimates hold:

$$\begin{cases}\dfrac{f_1}{\frac{1}{3}f_4}\le 6\,\dfrac{\rho^2m(d_1+d_2)^2s^2}{d_1d_2(m-1)}\le 6\,\dfrac{\rho^2m(d_1+d_2)^2C_1^2}{d_1d_2(m-1)}=1,\\[2ex] \dfrac{f_2}{\frac{1}{3}f_4}\le\dfrac{3\eta^2(m-1)}{2\rho^2\frac{d_1d_2}{m}}\le\dfrac{9\eta^2m^2(d_1+d_2)^2C_1^2}{(d_1d_2)^2}\le 1,\\[2ex] \dfrac{f_3}{\frac{1}{3}f_4}\le\dfrac{d_1d_2}{3(n+2)(d_1+d_2)C_1}\cdot\dfrac{3(n+2)C_1}{d_1}=\dfrac{d_2}{d_1+d_2}<1.\end{cases}$$

A.2. Gagliardo-Nirenberg interpolation and gradient estimate

By applying Lemmas 2 and 3, we obtain

$$\begin{aligned}\int_\Omega P^m\Psi(N)\le h\int_\Omega P^m&=h\|P^{\frac{m}{2}}\|_2^2\le hC_6\|P^{\frac{m}{2}}\|_{1,2}^{2\kappa}\|P^{\frac{m}{2}}\|_{\frac{2}{m}}^{2(1-\kappa)}\\ &\le hC_6\left(C_7\left(\frac{2}{m}\right)\right)^{2\kappa}\left(\|\nabla P^{\frac{m}{2}}\|_2+\|P^{\frac{m}{2}}\|_{\frac{2}{m}}\right)^{2(1-\kappa)}\\ &=hC_6\left(C_7\left(\frac{2}{m}\right)\right)^{2\kappa}\left(\|\nabla P^{\frac{m}{2}}\|_2+\|P^{\frac{m}{2}}\|_1\right)^{2(1-\kappa)}\\ &\le C_9\left(\|\nabla P^{\frac{m}{2}}\|_2^2+1\right)^{\kappa},\end{aligned}\tag{A.1}$$

which hold with some positive constant

$$\kappa=\frac{\frac{mn}{2}-\frac{n}{2}}{\frac{mn}{2}+1-\frac{n}{2}}\in(0,1).$$

Now from (3.8) and (A.1), we have

$$\int_\Omega P^{m-2}\Psi(N)|\nabla P|^2 \geq \int_\Omega P^{m-2}|\nabla P|^2 = \frac{4}{m^2}\int_\Omega |\nabla P^{\frac{m}{2}}|^2$$

$$\geq \frac{4}{m^2 C_9^{\frac{1}{\kappa}}}\left(\int_\Omega P^m\Psi(N)\right)^{\frac{1}{\kappa}} - \frac{4}{m^2}. \tag{A.2}$$

B. Technical estimates for Lemma 6

Estimation of P_1. For the first term P_1, we apply the semigroup estimate given in Lemma 1 to obtain

$$\|P_1(\cdot,t)\|_{L^\infty(\Omega)} \leq C_{13}\, t^{-\xi}e^{-\zeta t}\|P_0\|_{L^\infty(\Omega)}, \qquad t > 0, \tag{B.1}$$

where $\xi \in \left(\frac{n}{2q},\ 1\right)$ and $\zeta > 0$ are constants independent of t. Consequently, for all $t \in (\tau, T_{\max})$, we have

$$\|P_1(\cdot,t)\|_{L^\infty(\Omega)} \leq C_{13}\, \tau^{-\xi}\|P_0\|_{L^\infty(\Omega)}.$$

Estimation of P_2. For P_2, set $r = 0$, $q = n+2$, and $p = \infty$ in Lemma 1. We can then choose $\varrho \in \left(\frac{n}{2q}, \frac{1}{2}\right)$ and fix $\varepsilon \in \left(0, \frac{1}{2} - \varrho\right)$. It follows that there exist constants $C_{14} > 0$ and $\mu > 0$ such that

$$\begin{aligned}\|P_2(\cdot,t)\|_{L^\infty(\Omega)} &\leq C_3\, \|(A_{d_2}+1)^\varrho P_2(\cdot,t)\|_{L^q(\Omega)}\\ &\leq C_3\eta\int_0^t \|(A_{d_2}+1)^\varrho e^{-(t-s)(A_{d_2}+1)}\nabla\cdot(P(\cdot,s)\nabla N(\cdot,s))\|_{L^q(\Omega)}\,ds\\ &\leq C_{14}\int_0^t (t-s)^{-\varrho-\frac{1}{2}}e^{-(\mu+1)(t-s)}\|P(\cdot,s)\nabla N(\cdot,s)\|_{L^q(\Omega)}\,ds,\end{aligned} \tag{B.2}$$

for all $t \in (0, T_{\max})$. From (3.14), there exists a constant $C_{15} > 0$ such that

$$\|P(\cdot,t)\nabla N(\cdot,t)\|_{L^q(\Omega)} \leq C_{15}, \qquad \forall\, t \in (\tau, T_{\max}). \tag{B.3}$$

Substituting (B.3) into (B.2), we find

$$\begin{aligned}\|P_2(\cdot,t)\|_{L^\infty(\Omega)} &\leq C_{14}C_{15}\int_0^t (t-s)^{-\varrho-\frac{1}{2}}e^{-(\mu+1)(t-s)}\,ds\\ &\leq C_{14}C_{15}\int_0^\infty \sigma^{-\varrho-\frac{1}{2}}e^{-(\mu+1)\sigma}\,d\sigma\\ &\leq C_{16}\,\Gamma\left(\tfrac{1}{2}-\varrho-\varepsilon\right),\end{aligned} \tag{B.4}$$

where $\Gamma(\cdot)$ denotes the Gamma function. Since $\frac{1}{2} - \varrho - \varepsilon > 0$, the above quantity is positive and finite.

Estimation of P_3. Finally, for P_3, we apply Lemma 1 with $r = 1$, $q = n+2$, and $p \in (n, \infty]$. We can then choose $\varsigma \in \left(\frac{1}{2}\left(1 - \frac{n}{p} + \frac{n}{q}\right), 1\right)$. It follows that

$$\|P_3(\cdot,t)\|_{L^\infty(\Omega)} \leq C_3\, \|(A_{d_2}+1)^\varsigma P_3(\cdot,t)\|_{L^q(\Omega)}$$

$$
\begin{aligned}
&\le C_3C_4\int_0^t (t-s)^{-\varsigma}e^{-\nu(t-s)}\|h_2(N,P)+P\|_{L^q(\Omega)}\,ds\\
&\le C_3C_4\int_0^t (t-s)^{-\varsigma}e^{-\nu(t-s)}(m_2+\tfrac{\varepsilon a}{b}+\mu_2+E_2)\,\|P(\cdot,s)\|_{L^q(\Omega)}\,ds\\
&\le C_{17}\int_0^t (t-s)^{-\varsigma}e^{-\nu(t-s)}\,ds.
\end{aligned}
$$

By evaluating the integral and using the Gamma function identity, we obtain

$$\|P_3(\cdot,t)\|_{L^\infty(\Omega)} \le C_{18}\,\Gamma(1-\varsigma),$$

for some constant $C_{18} > 0$ independent of t.

AIMS Press